Final version available at Springer : http://dx.doi.org/10.1007/s10596-017-9687-3

Comparison between cell-centered and nodal based discretization schemes for linear elasticity

Halvor M. Nilsen · Jan Nordbotten · Xavier Raynaud

Received: date / Accepted: date

Abstract In this paper we study newly developed methods for linear elasticity on polyhedral meshes. Our emphasis is on applications of the methods to geological models. Models of subsurface, and in particular sedimentary rocks, naturally lead to general polyhedral meshes. Numerical methods which can directly handle such representation are highly desirable. Many of the numerical challenges in simulation of subsurface applications come from the lack of robustness and accuracy of numerical methods in the case of highly distorted grids. In this paper we investigate and compare the Multi-Point Stress Approximation (MPSA) and the Virtual Element Method (VEM) with regards to grid features that are frequently seen in geological models and likely to lead to a lack of accuracy of the methods. In particular we look at how the methods perform near the incompressible limit. This work shows that both methods are promising for flexible modeling of subsurface mechanics.

Keywords Multi-Point Stress Approximation · Virtual Element Method · Mimetic finite difference · Geomechanics · Linear elasticity · Polyhedral grids

1 Introduction

Modeling of sedimentary subsurface rock naturally leads to general unstructured grids because of stratigraphic layering, erosion and faults. The industry standard for grids in reservoir modeling is the Corner-Point grids (cp-grids).

H. Nilsen and X. Raynaud
SINTEF, Applied Mathematics and cybernetics, Oslo, Norway,
halvorMoll.nilsen@sintef.no, xavier.raynaud@sintef.no

J. Nordbotten
Department of Mathematics, University of Bergen, Norway
Department of Civil and Environmental Engineering, Princeton University, USA
jan.nordbotten@math.uib.no

Other geometrical grid formats have been proposed to improve on this format, but all compact representations of the underlying geology will lead to cells with high aspect ratios, distorted cells, large variations in cell volumes and faces areas. By compact, we mean a geometrical representation where the number of cells roughly corresponds to the number of physical parameters (such as rock properties). When physical parameters are assigned to a domain such as a reservoir, the connected regions that correspond to the same physical parameter are typically not finely meshed, and in the most compact possible representation, they are represented by a single cell. For very heterogeneous media such as reservoir, non-compact representations typically lead to very large grids that are computationally too demanding. Methods that are valid on general polyhedral grids and are robust for different grid types will greatly simplify the modeling of subsurface physics for multiphase flow encountered in the oil and gas industry. The workhorse method there is the finite volume discretization based on a two point flux approximation (TPFA). The method does not necessarily converge to the exact solution for general grids and can introduce large grid-orientation effects, see for example [20, Figure 3], but is very robust due to its monotonicity properties, which often result in faster computation times. The multi-point flux approximation (MPFA) method has been developed to solve the convergence problems and has been successfully applied to minimize grid-orientation effects [1, 15], but due to lack of monotonicity, the method remains difficult to apply to complex grids such as those arising from real reservoir models. Based on a mixed formulation, the mimetic finite difference method has been proposed for incompressible flow [9, 8], but problems arise in the case of fully compressible black oil models, as the method introduces non-monotonicity and significantly more degrees of freedom. In recent years, the coupling of geo-mechanical effects with subsurface flow has become more important in many areas including oil and gas production from mature fields, fractured tight reservoirs as well as geothermal application and risk assessment of CO2 injection. Realistic modeling of these geological cases is hampered by differences in the way geo-mechanics and flow models are built and discretized.

Recently, a cell-centered finite volume discretization has been proposed in [21] to specifically address problems arising in coupled geo-mechanical and flow simulation of porous media. The method is inspired from the MPFA discretization developed for flow problems and was thus named multi-point stress approximation (MPSA). The MPSA method presents two appealing features for subsurface applications. Since the method is based on the MPFA method, it shares the same data structure based on finite volume discretization, which is commonly used for the flow problem. Moreover, the method can operate on the general polyhedral grids that are typically used to represent complex heterogeneous medium. This later property is shared by the virtual element (VE) method [6]. The VE method builds upon the long-standing effort in the development of mimetic finite difference (MFD) methods, see [16, 5]. The MFD method reproduces at the discrete level fundamental properties of the differentiation operators, using only the available degrees of freedom and

without explicitly constructing the finite element basis. In this way, the method can easily handle general cell shapes. The VE method is a reformulation of the MFD method in the finite element framework. Both the MPSA and the VE methods for mechanics naturally define the divergence of the displacement on cells (see [23] for MPSA), which is also the natural coupling term between flow and mechanics, when flow is discretized with finite volume methods. As pointed out in [21], any attempt to extend the TPFA method to mechanics is bound to fail as the method already fails the local patch test. The local patch test verifies that the numerical method preserves rigid rotations, which are exact solutions to the problem.

In this paper we will investigate the MPSA and VE methods for mechanics with special emphasis on grid artifacts that are widespread in geological models of sedimentary rock reservoirs. Even if both aspects are related, our first interest is not the convergence properties of the methods but their performance on coarse and distorted meshes. This paper contains the first set of tests where the MPSA method is tested in view of applications to geosciences. In addition, we will discuss the properties of the methods in the incompressible limit since it has practical consequences for the short time dynamics of elasticity problems coupled with flow, as for example the Biot's equations. We also look at the different properties of the methods for different types of grids and how the methods can incorporate features like fractures.

2 Presentation of the methods

We study the methods for the standard equations of linear elasticity given by

$$\begin{aligned} \nabla \cdot \boldsymbol{\sigma} &= \boldsymbol{f}, \\ \boldsymbol{\varepsilon} &= \frac{1}{2}(\nabla + \nabla^T)\boldsymbol{u}, \\ \boldsymbol{\sigma} &= \boldsymbol{C}\boldsymbol{\varepsilon}, \end{aligned} \tag{1}$$

where $\boldsymbol{\sigma}$ is the Cauchy stress tensor, $\boldsymbol{\varepsilon}$ the infinitesimal strain tensors and $\boldsymbol{u}$ the displacement field. The linear operator $\boldsymbol{C}$ is a fourth-order stiffness tensor. For isotropic materials, we have the constitutive equations

$$\boldsymbol{\sigma} = 2\mu\boldsymbol{\epsilon} + \lambda \operatorname{trace}(\boldsymbol{\epsilon})\boldsymbol{I}, \tag{2}$$

where μ and λ denote the Lamé coefficients. We summarize the description of the methods given in [10] for the VE method and in [21] for MPSA. In the case of VE, we do not use the nodal representations of the load and traction terms. Instead we use traction and load terms defined on faces and cells, respectively. This is consistent with the physical meaning of these terms in addition to the fact that the integration rules hold exactly. The advantages of this evaluation for the volume force is discussed in [25].

2.1 The Virtual Element Method

As in the classical finite element method, the VE method starts from the linear elasticity equations written in the weak form

$$\int_\Omega \boldsymbol{\varepsilon}(\boldsymbol{v}) : \boldsymbol{C}\boldsymbol{\varepsilon}(\boldsymbol{u})\, dx = \int_\Omega \boldsymbol{v}\cdot\boldsymbol{f}\, dx \quad \text{for all} \quad \boldsymbol{v}. \tag{3}$$

In (3), we use the standard scalar product for matrices defined as

$$\boldsymbol{\alpha} : \boldsymbol{\beta} = \text{trace}(\boldsymbol{\alpha}^t\boldsymbol{\beta}) = \sum_{i,j=1}^{3} \boldsymbol{\alpha}_{i,j}\boldsymbol{\beta}_{i,j},$$

for any two matrices $\boldsymbol{\alpha}, \boldsymbol{\beta} \in \mathbb{R}^{3\times 3}$. We have also introduced the symmetric gradient $\boldsymbol{\varepsilon}$ given by

$$\boldsymbol{\varepsilon}(u) = (\nabla + \nabla^T)\boldsymbol{u},$$

for any displacement $\boldsymbol{u}$. The fundamental idea in the VE method is to compute on each element an approximation a_K^h of the bilinear form

$$a_K(\boldsymbol{u}, \boldsymbol{v}) = \int_K \boldsymbol{\varepsilon}(\boldsymbol{u}) : \boldsymbol{C}\boldsymbol{\varepsilon}(\boldsymbol{v})\, dx, \tag{4}$$

that, in addition to being symmetric, positive definite and coercive (uniformly with respect to the grid size if we want convergence), is also exact for linear functions. Note that in this paper, we only consider first-order methods. If higher order methods are used, the exactness must hold for polynomials of a given degree where the degree determines the order of the method. These methods were first introduced as mimetic finite element methods but later developed further under the name of virtual element methods (see [5] for discussions). The degrees of freedom are chosen as in the standard finite element methods to ensure the continuity at the boundaries and an element-wise assembly of the bilinear forms a_K^h. We have followed the implementation described in [10]. In a first-order VE method, the projection operator $\mathcal{P}$ into the space of linear displacement has to be computed locally for each cell. The VE approach ensures that it can be computed exactly for each basis element. The projection operator is defined with respect to the metric induced by the bilinear form a_K. The following orthogonal decomposition of the energy, which corresponds to Pythagoras identity, holds

$$a_K(\boldsymbol{u}, \boldsymbol{v}) = a_K(\mathcal{P}\boldsymbol{u}, \mathcal{P}\boldsymbol{v}) + a_K((\boldsymbol{I} - \mathcal{P})\boldsymbol{u}, (\boldsymbol{I} - \mathcal{P})\boldsymbol{v}) \tag{5}$$

for all displacement field $\boldsymbol{u}$ and $\boldsymbol{v}$ (In order to keep this introduction simple, we do not state the requirements on regularity which is needed for the displacement fields). In [10], an explicit expression for $\mathcal{P}$ is given so that we do not even have to compute the projection. Indeed, we have $\mathcal{P} = \mathcal{P}_R + \mathcal{P}_C$ where

$\mathcal{P}_R$ is the projection on the space R of pure rotations and $\mathcal{P}_C$ the projection on the space C of constant shear strain. The spaces R and C are defined as

$$R = \left\{ \boldsymbol{a} + B(\boldsymbol{x} - \bar{\boldsymbol{x}}) \mid \boldsymbol{a} \in \mathbb{R}^3, B \in \mathbb{R}^{3\times 3}, B^T = -B \right\},$$
$$C = \left\{ B(\boldsymbol{x} - \bar{\boldsymbol{x}}) \mid B \in \mathbb{R}^{3\times 3}, B^T = B \right\}.$$

Then, the discrete bilinear form a_K^h is defined as

$$a_K^h(\boldsymbol{u}, \boldsymbol{v}) = a_K(\mathcal{P}\boldsymbol{u}, \mathcal{P}\boldsymbol{v}) + s_K((\boldsymbol{I} - \mathcal{P})\boldsymbol{u}, (\boldsymbol{I} - \mathcal{P})\boldsymbol{v}) \tag{6}$$

where s_K is a symmetric positive matrix which is chosen such that a_K^h remains coercive. Note the similarities between (6) and (5). Since $\mathcal{P}_R$ and $\mathcal{P}_C$ are orthogonal and $\mathcal{P}_R$ maps into the null space of a_K (rotations do not produce any change in the energy), we have that the first term on the right-hand side of (5) and (6) can be simplified to

$$a_K(\mathcal{P}\boldsymbol{u}, \mathcal{P}\boldsymbol{v}) = a_K(\mathcal{P}_C\boldsymbol{u}, \mathcal{P}_C\boldsymbol{v}).$$

The expression (6) immediately guarantees the consistency of the method, as we get from (6) that, for linear displacements, the discrete energy coincides with the exact energy. Since the projection operator can be computed exactly for all elements in the basis - and in particular for the *virtual* basis elements for which we do not have explicit expressions - the local matrix can be written only in terms of the degrees of freedom of the method. In our case the degrees of freedom of the method are the value of displacement at the node. Let us denote $\boldsymbol{\varphi}_i$ a basis for these degrees of freedom. The matrix $(\boldsymbol{A}_K)_{i,j} = a_K(\boldsymbol{\varphi}_i, \boldsymbol{\varphi}_j)$ is given by

$$\boldsymbol{A}_K = |K|\boldsymbol{W}_C^T\boldsymbol{D}\boldsymbol{W}_C + (\boldsymbol{I} - \boldsymbol{P})^T\boldsymbol{S}_K(\boldsymbol{I} - \boldsymbol{P}). \tag{7}$$

In (7), $\boldsymbol{W}_C$ is the projection operator from the values of node displacements to the space of constant shear strain and $\boldsymbol{S}_K$, which corresponds to a discretization of s_K in (6), is a symmetric positive matrix which guarantees the positivity of $\boldsymbol{A}_K$. There is a large amount of freedom in the choice of $\boldsymbol{S}_K$ but it has to be scaled correctly. We choose the same S_K as in [10]. The matrix $\boldsymbol{D}$ in (7) corresponds to the tensor $\boldsymbol{C}$ rewritten in Voigt notations so that, in three dimensions, we have

$$\boldsymbol{D}_{ij} = \boldsymbol{\varepsilon}_i : \boldsymbol{C}\boldsymbol{\varepsilon}_j, \qquad \text{for } i, j = 1, \ldots, 6.$$

Finally, the matrices $\boldsymbol{A}_K$ are used to assemble the global matrix $\boldsymbol{A}$ corresponding to a^h.

2.2 Multi-Point Stress Approximation

The Multi-Point Stress Approximation (MPSA) is inspired from the MPFA method [1] which is a finite volume method for fluid flow. Its derivation is based on discrete principles for the conservation of momentum and the continuity of the forces. We use the same notations as in [22], which are also summarized in

Table 1 Notations used in the presentation of the MPSA method.

K, σ, s	: Generic notation for a cell, a face or a vertex, respectively
$\mathcal{T}_\sigma$, $\mathcal{T}_s$	: set of cells which contains the face σ and the vertex s, respectively
$\mathcal{F}_K$, $\mathcal{F}_s$	: set of faces which belong the cell K and the vertex s, respectively
$\mathcal{V}_K$, $\mathcal{V}_\sigma$	: set of vertices that belong to the cell K and the face σ, respectively
K_s	: Interaction region of the cell K with the vertex s
γ	: Generic notation for a subface. Given $\sigma \in \mathcal{F}_s$, γ_s^σ is the subface contained in σ which contains the vertex s.
I_s	: interaction region corresponding to the vertex s, i.e. $I_s = \cup K_s$ for $K \in \mathcal{T}_s$.
$\boldsymbol{u}_K$	: displacement at cell center K
$\boldsymbol{x}_K$	: cell center
$\boldsymbol{x}_s^{\sigma,\beta}$	: location of the Gauss points of the subface γ_s^σ
$\boldsymbol{u}_{K,s}^{\sigma,\beta}$	: displacement at the Gauss points $\boldsymbol{x}_s^\sigma$, on the side of the cell K (we allow $\boldsymbol{u}_{K,s}^{\sigma,\beta} \neq \boldsymbol{u}_{K',s}^{\sigma,\beta}$, for $\sigma = K \cap K'$)
$\boldsymbol{u}_{K,s}^{\sigma}$	: displacement at subface γ_s^σ computed from the values at the Gauss points using (8)
$n_{K,\sigma}$	: normal to the face σ pointing outwards from K.
$\boldsymbol{T}_{K,s}^{\sigma}$	: force at the subface $\sigma_{K,s}$ evaluated from K_s (we allow for $\boldsymbol{T}_{K,s}^{\sigma} \neq \boldsymbol{T}_{K',s}^{\sigma}$, for $\sigma = K \cap K'$)
$N_{K,s}^{\mathcal{F}}$	: number of subfaces γ_s^σ, with $\sigma\mathcal{F}_K \cap \mathcal{F}_s$ for a given interaction region K_s
$N_s^{\mathcal{T}}, N_s^{\mathcal{F}}$	: number of cells and faces, respectively, which contain s

Table 1 and Figure 1 (Note that σ in this section no longer denotes the Cauchy stress tensor but a face of a cell). Each cell K is divided into interaction subregions, one for each vertex s of the cell K. We denote such subregion as K_s. An interaction region for a vertex s, denoted I_s, is defined as the union of the subregions of the cells that share the vertex s. This partition induces a partition of the faces in subfaces, which we generically denote by γ. For a face $\sigma = K \cap K'$, the subface γ_s^σ is given by $K_s \cap K_s'$. On the subface γ_s^σ, we consider a set of Gauss points, $\boldsymbol{x}_s^{\sigma,\beta}$ for $\beta \in \{1, \ldots, k\}$. We require that we have enough Gauss points to obtain a second order approximation (In 2D, this can be obtained for $k = 2$ which is also our choice in the implementation). We can compute an approximation of the value of the displacement on the subface $\sigma_{K,s}$ given the values at the Gauss point by using the quadrature formula

$$\boldsymbol{u}_{K,s}^{\sigma} = \sum_{\beta=1}^{k} \omega_\beta \boldsymbol{u}_{K,s}^{\sigma,\beta}, \tag{8}$$

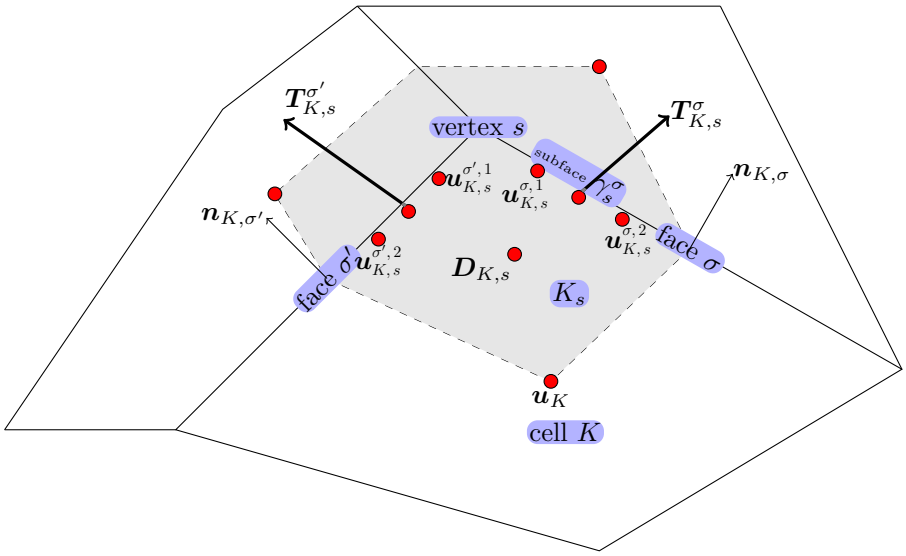

Fig. 1 Illustration picture for the MPSA method. The interaction region for the vertex s is represented in gray. See Table 1 for the notations.

where ω_β denotes the Gauss quadrature weights. A linear approximation of $\boldsymbol{u}$ in a subregion K_s is defined by the value of $\boldsymbol{u}_K$ at the cell center and a linear mapping denoted $\boldsymbol{D}_{K,s} \in \mathbb{R}^{d\times d}$ which corresponds to the gradient of the linear approximation. Given a linear approximation in a subregion, the values of $\boldsymbol{u}$ at the Gauss points is given by

$$\boldsymbol{u}^{\sigma,\beta}_{K,s} := \boldsymbol{u}(\boldsymbol{x}^{\sigma,\beta}_s) = \boldsymbol{u}_K + \boldsymbol{D}_{K,s}(\boldsymbol{x}^{\sigma,\beta}_s - \boldsymbol{x}_K). \tag{9}$$

and we denote by $G_{K,s}$ the corresponding mapping,

$$\begin{aligned} G_{K,s} &: \mathbb{R}^{d(d+1)} \to \mathbb{R}^{dkN^{\mathcal{F}}_{K,s}} \\ \boldsymbol{u}_K, \{\boldsymbol{D}_{K,s}\} &\mapsto \left\{\boldsymbol{u}^{\sigma,\beta}_{K,s}\right\}_{\substack{\sigma\in\mathcal{F}_s\cap\mathcal{F}_K \\ \beta=\{1,\dots,k\}}}. \end{aligned} \tag{10}$$

See Figure 2 for a schematic representation of the mappings that are introduced in this section. Given a linear approximation, we can also compute the stress field using Hooke's law (2) and define the force on each subface as

$$\boldsymbol{T}^{\sigma}_{K,s} = m^s_\sigma \left(\mu_K(\boldsymbol{D}_{K,s} + \boldsymbol{D}^t_{K,s}) + \lambda_K(\mathrm{trace}(\boldsymbol{D}_{K,s}))I\right)\cdot \boldsymbol{n}_{K,\sigma}. \tag{11}$$

In (11), m^σ_s denotes the area of the subface γ^σ_s. In this way, we define the mapping $T_{K,s}$ that maps gradient to subface forces as

$$\begin{aligned} T_{K,s} &: \mathbb{R}^{d\times d} \to \mathbb{R}^{d\,N^{\mathcal{F}}_{K,s}} \\ \boldsymbol{D}_{K,s} &\mapsto \left\{\boldsymbol{T}^{\sigma}_{K,s}\right\}_{\sigma\in\mathcal{F}_s\cap\mathcal{F}_K} \end{aligned} \tag{12}$$

Finally, we introduce the reconstruction operator R_s which, from cell values in an interaction region, yields a linear approximation in each interaction subregion (in form of a matrix),

$$\begin{aligned} &R_s \colon \mathbb{R}^{dN_s^{\mathcal{T}}} \to \mathbb{R}^{d\,N_s^{\mathcal{T}}(d+1)} \\ &\{\boldsymbol{u}_K\}_{K\in\mathcal{T}_s} \mapsto \{\boldsymbol{u}_K\}_{K\in\mathcal{T}_s}, \{\boldsymbol{D}_{K,s}\}_{K\in\mathcal{T}_s}. \end{aligned} \tag{13}$$

The mapping R_s is largely undertermined in the sense that there are many coefficients that remain to be set. We exploit these degrees of freedom in choosing the coefficients of R to enforce the continuity of the forces at each subface and minimize the jump of the displacement field at the Gauss points. The continuity of the forces at each subface is given by

$$\boldsymbol{T}_{K,s}^{\sigma} = -\boldsymbol{T}_{K',s}^{\sigma} \tag{14}$$

whenever $\sigma = K \cap K'$. The values of $\boldsymbol{T}_{K,s}^{\sigma}$ are computed using (11). We define a measure of the jump of displacement at the subfaces as

$$J_s = \sum_{\sigma\in\mathcal{F}_s} \sum_{\beta\in\{1,2\}} \sum_{K,K'\in\mathcal{T}_\sigma} w_{K'.K} \left| \boldsymbol{u}_{K',s}^{\sigma,\beta} - \boldsymbol{u}_{K,s}^{\sigma,\beta} \right|^2. \tag{15}$$

The weights $w_{K,K'}$ in (15) can be chosen as the harmonic mean of the largest eigenvalue of the stiffness tensor $\boldsymbol{C}$ of the adjacent cells K and K', see [21, 22]. We introduce the vector $\boldsymbol{v}_s \in \mathbb{R}^{d\,N_s^{\mathcal{T}}}$ that consists of all the cell values of the displacement in the interaction region, $\boldsymbol{v}_s = [\boldsymbol{u}_{K_1}, \ldots, \boldsymbol{u}_{K_{N_s^{\mathcal{T}}}}]$. We denote by $\boldsymbol{d}_{K,s} \in \mathbb{R}^{d^2}$ the vector representation of the matrix $\boldsymbol{D}_{K,s} \in \mathbb{R}^{d\times d}$ and set $\boldsymbol{d}_s = [\boldsymbol{d}_{K_1}, \ldots, \boldsymbol{d}_{K_{N_s^{\mathcal{T}}}}]$. The definition of R_s now boils down to determining the values of $\boldsymbol{d}_s$ (the gradients in the interaction region), given the values of $\boldsymbol{v}_s$ (the displacements at the cell center). We can check from (11) that the condition (14) is linear and can be rewritten as

$$\boldsymbol{A}\boldsymbol{d}_s = 0$$

for some matrix $\boldsymbol{A} : \mathbb{R}^{d^2 N_s^{\mathcal{T}}} \to \mathbb{R}^{N_s^{\mathcal{F}}}$. We denote by $\delta\boldsymbol{u} \in \mathbb{R}^{dkN_s^{\mathcal{F}}}$ the vector whose components are given by the jumps of the Gauss points,

$$\delta\boldsymbol{u} = \left\{ \boldsymbol{u}_{K',s}^{\sigma,\beta} - \boldsymbol{u}_{K,s}^{\sigma,\beta} \right\}_{\substack{\sigma\in\mathcal{F}_s, K\in\mathcal{T}_s \\ \beta=\{1,2\}}}$$

We can then rewrite J_s as

$$J_s = \frac{1}{2}\delta\boldsymbol{u}^t \boldsymbol{M} \delta\boldsymbol{u}$$

where $\boldsymbol{M}$ is a diagonal symmetric positive definite matrix. The value at the Gauss points depends linearly on the coefficients of $\boldsymbol{D}_{K,s}$ and the values of $\boldsymbol{u}_L$, see (9). Therefore, using the representation $\boldsymbol{d}_s$ and $\boldsymbol{v}_s$, we end up with a relation of the type

$$\delta\boldsymbol{u} = \boldsymbol{B}\boldsymbol{d}_s + \boldsymbol{E}\boldsymbol{v}_s \tag{16}$$

for some matrices $\boldsymbol{B} : \mathbb{R}^{d^2 N_s^{\mathcal{T}}} \to \mathbb{R}^{2kdN_s^{\mathcal{F}}}$ and $\boldsymbol{E} : \mathbb{R}^{dN_s^{\mathcal{T}}} \to \mathbb{R}^{2kdN_s^{\mathcal{F}}}$. Using (16), we get

$$J_s = \frac{1}{2}\boldsymbol{d}_s^t \boldsymbol{B}^t \boldsymbol{M} \boldsymbol{B} \boldsymbol{d}_s + \boldsymbol{d}_s^t \boldsymbol{B}^t \boldsymbol{M} \boldsymbol{E} \boldsymbol{v}_s + \frac{1}{2}\boldsymbol{v}_s^t \boldsymbol{E}^t \boldsymbol{M} \boldsymbol{E} \boldsymbol{v}_s \tag{17}$$

We set $\boldsymbol{d}_s$ as the minimizer of J_s, with respect to $\boldsymbol{d}_s$, subject to the constraint $\boldsymbol{A}\boldsymbol{d}_s = 0$. We solve this quadratic minimization problem by using Lagrangian multipliers and setting up the corresponding saddle-point equations. We end up with an expression of the form $\boldsymbol{d}_s = \boldsymbol{R}_s \boldsymbol{v}_s$. This matrix $\boldsymbol{R}_s$ then defines the reconstruction operator R_s. Combining R_s and $T_{K,s}$ for each cell $K \in \mathcal{T}_s$, we can define the mapping T_s which, from cell values, computes the values of the force at the subfaces. For a subface γ_s^σ, we denote the force acting at this subface by $\boldsymbol{T}_s^\sigma$. Since the method imposes the continuity of the force, this value is now well-defined. We denote by T_s the mapping that compute the forces in the interaction region from cell-valued displacement,

$$\begin{aligned} T_s &: \mathbb{R}^{dN_s^{\mathcal{T}}} \to \mathbb{R}^{dN_s^{\mathcal{F}}} \\ \{\boldsymbol{u}_K\}_{K\in\mathcal{T}_s} &\mapsto \{\boldsymbol{T}_s^\sigma\}_{\sigma\in\mathcal{F}_s}. \end{aligned} \tag{18}$$

The mapping T_s can be written in the form

$$\boldsymbol{T}_{K,s}^\sigma = \sum_{K'\in\mathcal{T}_s} t_{K,K',s,\sigma} \boldsymbol{u}_{K'}. \tag{19}$$

The local coefficient tensors $t_{K,K',s,\sigma}$ are referred to as subface stress weight tensors, and generalize the notion of transmissibilities from the scalar diffusion equation [21]. The system of equations for linear elasticity are then given by the discrete conservation of momentum. It means that, for each cell, the sum of the forces applied to all faces is equal to the external force applied to the cell, that is

$$\sum_{\sigma\in\mathcal{F}_K} \boldsymbol{T}_K^\sigma = \int_K \boldsymbol{f}(\boldsymbol{x})\, d\boldsymbol{x}. \tag{20}$$

The force acting on a cell-face is naturally defined as the sum of the forces acting on all the corresponding subfaces, that is

$$\boldsymbol{T}_K^\sigma = \sum_{\{s\in\mathcal{V}_\sigma\}} \boldsymbol{T}_{K,s}^\sigma \tag{21}$$

where $\mathcal{V}_\sigma$ denote the set of vertices that belong to the face σ.

2.3 Fundamental differences between the methods

There are fundamental differences between VEM and MPSA in the assembly process. In the VE framework, the matrix $\boldsymbol{A}$ defining the discrete equation $\boldsymbol{A}\boldsymbol{u} = \boldsymbol{f}$ is computed element for element, based on rock parameters and the geometry of the cell. In the MPSA method, we first calculate the forces

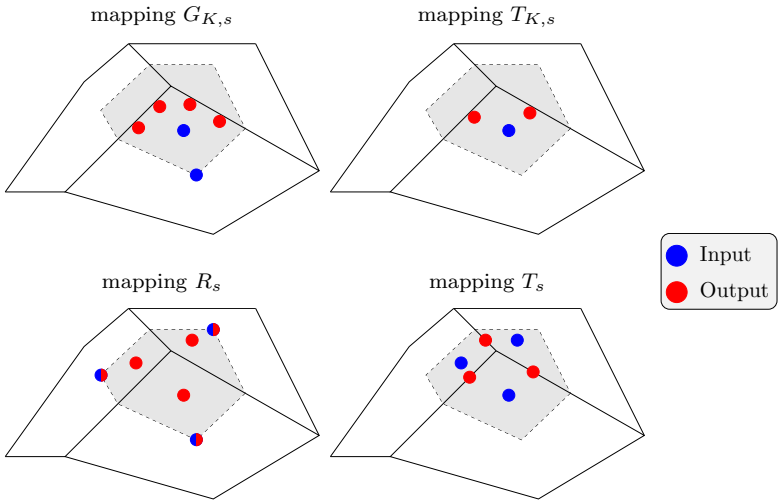

Fig. 2 schematic representation of the mappings used in the derivation of MPSA. Here we use the same interaction region as in Figure 1 and give the locations of the input and outputs for each mapping.

from cell center displacement. This calculation requires solving a constrained quadratic minimization problem, which in our implementation is resolved by solving a linear saddle-point system. For certain grids, a singular value decomposition is required to eliminate redundant constraints. Then the contribution to a matrix element is calculated by summing up the contributions from each subface. So VE operates on the element, while MPSA operates on interaction regions. Note that the set of interaction regions, considered as cells, will constitute a dual grid of the original grid. Recently, a new variant of the MPSA method has been developed in [12], based on ideas from weakly symmetric mixed finite element discretizations. This new variant leads to a simpler local problem, since the weakly imposed symmetry allows for well-posed local problems using only a single continuity point on each face. Thus there are equal number of constraints as degrees of freedom, and the local minimization problems are replaced by simpler (and smaller) linear systems.

2.3.1 Comparison of the method with respect to grid features

In the context of geosciences, the MPSA method has the advantage to allow for an easy treatment of fractures. A fracture appearing at the interface between two cells can be modeled in a straightforward way by decoupling the corresponding face. If we denote this face by σ, Equation (14) is replaced by $\boldsymbol{T}^{\sigma}_{K,s} = 0 = -\boldsymbol{T}^{\sigma}_{K',s}$ and the displacement values at the Gauss points, $\boldsymbol{u}^{\sigma,\beta}_{K,s}$ and $\boldsymbol{u}^{\sigma,\beta}_{K',s}$ for $K, K' \in \mathcal{T}_{\sigma}$ are removed from the sum in (15). The method, before removing the degrees of freedom, is similar to a mixed method. This can be seen more explicitly in [12], where the MPSA method which is presented there

is very similar to the PEERS elements for triangles [3]. The difference is that the PEERS elements have one set of forces on edges and an addition bubble function to obtain stability for the incompressible limit, while the MPSA method has two sets of forces on the edges. To reduce the degrees of freedom of the global system, the MPSA method sacrifices the symmetry and positive definiteness of the local systems. In the case of triangles, there exists a symmetric block diagonal inner-product as noticed in [17], which makes the formulation [12] attractive.

The disadvantages of the MPSA method is that it is not symmetric and only conditionally stable, a property which is also encountered in the MPFA method [17, 14]. It may result in failure or poor results for severely distorted grids, and strongly anisotropic media. However, the stability of the method can be verified locally [22]. Still, this may prevent it from being used on specific grids without extra griding. Generally the MPSA will suffer from the same grid restrictions as MPFA. The method also requires the inversion of local matrices, which may induce an extra cost, but this only affects the assembly process, which is only done at the beginning of a simulation if the physical parameters remain unchanged. In the case of VEM, we can expect the same structure as for FEM so that the same solvers can be used. The system matrix is by construction symmetric, positive and definite. If not modified, the VE method suffers from the same limitations with respect to locking and accuracy of stresses as a linear FE method. In addition, forces are not as naturally defined on faces as they are in MPSA and methods of mixed type. Some of these problems can be avoided by using techniques developed for FEM solutions [26] since for simple grids the VE and FE methods become equivalent.

2.3.2 Limit of incompressible elasticity

In the limit of incompressible elasticity, the displacement field tends to be solenoidal, that is, divergence free. Numerical locking occurs when solenoidal fields are poorly approximated at the discrete level. In the context of subsurface application, numerical locking will be an issue when considering the coupling of linear elasticity for the rock matrix with flow. To see that, let us consider the Biot's equations [7] which are commonly used in the simulation of hydromechanical problems. The Biot's equations consist of the following linear equations,

$$\nabla \cdot \boldsymbol{\sigma} + \alpha \nabla p = \boldsymbol{f}, \tag{22a}$$

$$\frac{\partial}{\partial t}(c_0 p + \alpha \nabla \cdot \boldsymbol{u}) + \nabla \cdot (\boldsymbol{K} \nabla p) = 0, \tag{22b}$$

$$\boldsymbol{\varepsilon} = \frac{1}{2}(\nabla + \nabla^T)\boldsymbol{u}, \tag{22c}$$

$$\boldsymbol{\sigma} = \boldsymbol{C}\boldsymbol{\varepsilon}, \tag{22d}$$

where $c_0 p + \alpha \nabla \cdot \boldsymbol{u}$ denotes the fluid content. The fluid content depends on the fluid pressure p and on the rock volume change given by $\nabla \cdot \boldsymbol{u}$ which is

weighted by the Biot-Willis constant α. We discretize in time the equations (22) and use a superscript n to denote the values corresponding to the time step n. From (22), we get

$$\nabla \cdot \boldsymbol{\sigma}^{n+1} + \alpha \nabla p^{n+1} = \boldsymbol{f}^{n+1}, \tag{23a}$$

$$c_0 p^{n+1} + \alpha \nabla \cdot \boldsymbol{u}^{n+1} + \Delta t \, \nabla \cdot (\boldsymbol{K} \nabla (p^{n+1})) = c_0 p^n + \alpha \nabla \cdot \boldsymbol{u}^n, \tag{23b}$$

$$\boldsymbol{\varepsilon}^{n+1} = \frac{1}{2}(\nabla + \nabla^T)\boldsymbol{u}^{n+1}, \tag{23c}$$

$$\boldsymbol{\sigma}^{n+1} = \boldsymbol{C}\boldsymbol{\varepsilon}^{n+1}. \tag{23d}$$

In equation (23b), we can see that, in the limit where the fluid becomes incompressible, that is $c_0 \approx 0$, when the time-step Δt tends to zero, the change in the divergence of $\boldsymbol{u}$ becomes very small. In this case, we are computing a displacement field which is close to solenoidal and numerical locking becomes an issue.

In the case of VEM and any finite element method, the material parameters enter the discrete equations *cell-wise* in the assembly of the bilinear form a, see (6). Letting λ be very large compared to μ therefore imposes a near solenoidality condition on each cell. To evaluate the level of locking, we can compare the number of degree of freedom of the whole system with the number of local solenoidal equations, that is, the equations which locally impose the solenoidal condition for large λ. The heuristic is then the following: If the number of local solenoidal equations is small with respect to the number of degree of freedoms, then there are potentially enough degrees of freedom left after having fulfilled the solenoidal equations to approximate the actual solution. We avoid also the appearance of spurious modes which is characteristic for locking, see [5, section 8.3] where this aspect is discussed for the Stokes equation. Such counting arguments to assess the well-posedness of a system, which consists of comparing the number of degree of freedom and the number of *near* constraint, have been used in the literature earlier, see e.g. [19]

In the case of VEM, the ratio between the number of cells and the number of nodes will give an indication of the sensitivity of the grid with respect to locking. The higher this ratio is, the more likely it is that locking appears. Hence, triangular grid, where this ratio is high, are likely to lock. One has to introduce extra face degrees of freedom and the restriction is the same as for the case of the linear Stokes equations. A sufficient condition for avoiding locking in 2D is that each corner have only three faces without extra degrees of freedom. On the other side, PEBI grid (also called Voronoi meshes) where this ratio is low will not be likely to lock. We refer to [5] for a detailed analysis of the necessary conditions to avoid locking. In the case of the MPSA method, the situation is the opposite. The discrete representation of the stress tensor is done at each node so that the solenoidality condition will be imposed there. Therefore, the ratio between the number of interaction regions (which is also equal to the number of nodes) with the number of cells (which corresponds to the number of degree of freedom for MPSA) will determine the sensitivity of the grid to locking. A PEBI grid will then much more likely lead to locking

than a triangular grid. More generally, we can conclude that the grids where the MPSA method and the VE method lock are dual grids of each other. In the case of many geological applications, the compressibility of water is about the same as of the rock, which means that locking is not happening. Indeed in that case the effective second Lamé parameter is $\lambda + \frac{1}{c_0}$, which is of the same order of magnitude than μ. However, for mud and shale, it may be important as $\lambda \gg \mu$.

It seems that the limitations with respect to locking are a bit less severe for MPSA. However, it is important in this case to resolve the local minimization problems, see (17), with sufficient accuracy so that the div-free part of the solution is well preserved, since this part will be multiplied with a large parameter. In the discretization of the Biot's equations in the framework of MPSA, a regularization-like term arises naturally by recognizing that the numerical divergence for displacement depends on pressure. This can be seen from the discretization in the reduction to cell-centered variables. The essential ingredients are that the divergence operator is defined in terms of displacement at cell boundaries and that the continuity of forces is required by using the effective stress, that is $\boldsymbol{\sigma} - \alpha p \boldsymbol{I}$, and not the continuity of the forces due to stress with an additional force from the pressure gradient. This requires that the discretization of the mechanics and the pressure system is done together. We also note that the discretization of the coupling is independent of the discretization of the gradient in the Darcy equation.

2.3.3 Regularization methods for the near-incompressible limit

We have implemented different regularization strategies to handle materials close to the near incompressible limit. For VEM, our approach follows [4] even if the results there hold for elements of order $k \geq 2$ while we only consider linear elements, that is $k = 1$. We will comment on that later. We use the constitutive equation given by (2) and the energy in a cell K is given by

$$\frac{1}{2} a_K(\boldsymbol{u}, \boldsymbol{u}) = \mu \int_K \boldsymbol{\varepsilon}(\boldsymbol{u}) : \boldsymbol{\varepsilon}(\boldsymbol{u})\, dx + \frac{\lambda}{2} \int_K |\nabla \cdot \boldsymbol{u}|^2 \, dx. \tag{24}$$

We introduce

$$a_{\mu,K}(\boldsymbol{u}, \boldsymbol{v}) = \int_K \boldsymbol{\varepsilon}(\boldsymbol{u}) : \boldsymbol{\varepsilon}(\boldsymbol{u})\, dx$$

so that (24) can be rewritten as

$$a_K(\boldsymbol{u}, \boldsymbol{u}) = 2\mu\, a_{\mu,K}(\boldsymbol{u}, \boldsymbol{u}) + \lambda \int_K |\nabla \cdot \boldsymbol{u}|^2 \, dx \tag{25}$$

The coercivity of a_K follows from the coercivity of $a_{\mu,K}$ but it deteriorates when λ get very large compared to μ. In terms of the Poisson ratio ν, we have

$$\frac{\mu}{\lambda} = \frac{1 - 2\nu}{2\nu} \tag{26}$$

so that the deterioration of the coercivity occurs when ν tends to $\frac{1}{2}$. In this case, the exact solution will be very close to a solenoidal field. As mentioned before, numerical locking occurs when too many degrees of freedom are used to satisfy the solenoidal constraint so that too few are left to approximate close-to-solenoidal solutions. Instead of (25), we consider the following approximation of a_K,

$$a_{K,\text{app}}(\boldsymbol{u},\boldsymbol{v}) = 2\mu\, a_{\mu,K}(\boldsymbol{u},\boldsymbol{v}) + \lambda \int_K |\Pi_{0,K}(\nabla\cdot\boldsymbol{u})|^2 \, dx. \tag{27}$$

Here $\Pi_{0,K}$ is the L^2 projection. When λ becomes very large, the strong penalization of the term following λ in (27) will impose on the solution the constraint

$$\Pi_{0,K}(\nabla\cdot\boldsymbol{u}) = 0 \tag{28}$$

while, for (25), it gave $\nabla\cdot\boldsymbol{u} = 0$. We have in this way relaxed the system as the constraint (28) is easier to fulfill than the solenoidal constraint $\nabla\cdot\boldsymbol{u} = 0$ (the latter implies the former, but not the other way around). More degrees of freedom are therefore left to resolve the rest of the displacement field. At the same time, we commit a *variational crime* meaning that we base our formulation on a non-exact form of the energy. However, in the VE method, the energy we consider is already an approximation because of the stabilization term and we are going to see that we retain exactness in the case of solutions corresponding to linear displacement, even when we use the relaxed version. To approximate $a_{\mu,K}$, we use the projection $\mathcal{P}$ and introduce a stabilization term as described in Section 2.1, that is,

$$a^h_{\mu,K}(\boldsymbol{u},\boldsymbol{v}) = a_{\mu,K}(\mathcal{P}\boldsymbol{u},\mathcal{P}\boldsymbol{v}) + s_{\mu,K}((\boldsymbol{I}-\mathcal{P})\boldsymbol{u},(\boldsymbol{I}-\mathcal{P})\boldsymbol{v}). \tag{29}$$

Then, the discrete approximation of the energy is given by

$$a^h_K(\boldsymbol{u},\boldsymbol{u}) = 2\mu\, a^h_{\mu,K}(\boldsymbol{u},\boldsymbol{u}) + \lambda \int_K |\Pi_0\nabla\cdot\boldsymbol{u}|^2 \, dx. \tag{30}$$

As usual the total energy will obtained by summing up the cell contributions,

$$a^h(\boldsymbol{u},\boldsymbol{v}) = \sum_{K\in\mathcal{T}} a^h_K(\boldsymbol{u},\boldsymbol{v}). \tag{31}$$

We can check that $\Pi_0(\nabla\cdot\boldsymbol{u})$ can be computed exactly for all elements of the virtual basis. Indeed to compute the L^2 projection of $\nabla\cdot\boldsymbol{u}$, we only need to evaluate its zero moment, that is, the integral of $\nabla\cdot\boldsymbol{u}$. A straightforward integration by parts give us

$$\int_K \nabla\cdot\boldsymbol{u}\, dx = \int_{\partial K} \boldsymbol{u}\cdot\boldsymbol{n}\, dx \tag{32}$$

and, by construction, for any $\boldsymbol{u}$ which belongs to the virtual basis, $\boldsymbol{u}$ is linear on the edges so that the integral on the right-hand side above can be computed

exactly. Thus, the bilinear form a_K^h in (30) can be assembled and the corresponding system inherits the consistency property of the VE method. Namely, if $\boldsymbol{u}$ is linear and $\boldsymbol{v}$ is one of the virtual basis element, then

$$a_K^h(\boldsymbol{u}, \boldsymbol{v}) = a_{K,\text{app}}(\boldsymbol{u}, \boldsymbol{v}). \tag{33}$$

We define a discrete divergence operator from node to cell variables as

$$\sum_{K\in\mathcal{T}} \mathtt{q}_K \mathtt{div}(\mathtt{u})_K = \sum_{K\in\mathcal{T}} \mathtt{q}_K \int_K \nabla\cdot\boldsymbol{u}\, dx$$

for all $\mathtt{q}_K$. Here $\boldsymbol{u}$ is the function in the virtual finite element space corresponding to the nodal displacement coefficients given by $\mathtt{u}$. We assemble the matrix $\mathtt{A}$ corresponding to the bilinear form a_μ^h in the same way as in section 2.1. We obtain that, for any discrete nodal displacement vector $\mathtt{u}$, the discrete bilinear form a^h takes the form

$$a^h(\boldsymbol{u}, \boldsymbol{u}) = \mu\, \mathtt{u}^T\mathtt{A}\mathtt{u} + \frac{\lambda}{2}\left|\mathtt{div}(\mathtt{u})\right|^2.$$

The discrete system of equations is obtained by taking the variation of a^h and we get

$$2\mu\mathtt{A}\mathtt{u} + \lambda\mathtt{div}^T\mathtt{div}(\mathtt{u}) = \mathtt{f},$$

for a given right-hand side $\mathtt{f}$. We can rewrite this system as

$$2\mu\mathtt{A}\mathtt{u} + \mathtt{grad}(\mathtt{p}) = \mathtt{f} \tag{34a}$$

$$\mathtt{div}(\mathtt{u}) - \frac{1}{\lambda}\mathtt{p} = 0, \tag{34b}$$

where $\mathtt{grad} = \mathtt{div}^T$. Then, $\mathtt{p}$ can then be interpreted as a pressure. This strategy where the solenoidal constraint is relaxed using a projection operator can be successfully applied when considering higher order method virtual finite element methods. Indeed, in [4], it is shown that for a method of order k is the projection operator Π_{k-2} is used for relaxation then the method is unconditionally convergent with respect to the parameter λ. Since we consider linear elements, that is $k = 1$, such operator is not available. Therefore, we need to introduce additional degree of freedom, in addition to the nodal values of displacement. In [5], it is shown that it is only necessary to introduce an extra edge degree of freedom for edges which connect to nodes that have more than three edges. The following three VE methods have been implemented,

VEM:	Standard implementation, as described in Section 2.1,
VEM-relax:	Implementation using the relaxed version coming from (30), see (34),
VEM-relax-extra:	Same as *VEM-relax* but we introduce an extra degree of freedom on each face so that the stability condition given in [5] is fulfilled.

For the MPSA method, a regularization of a similar nature is presented in [21] in the case of the poro-elastic equation. We detail its application to the incompressible limit. We use the same framework and notations as given in Section 2.2. The essential ingredient in [21] is to add to each cell K an extra degree of freedom p_K to approximate the divergence term $\lambda_K \nabla \cdot \boldsymbol{u}$ in the cell K. We replace the definition (11) of the forces on subfaces as

$$\boldsymbol{T}^{\sigma}_{K,s} = m^s_{\sigma} \left(\mu_K (\boldsymbol{D}_{K,s} + \boldsymbol{D}^t_{K,s}) + \lambda_K p_K \boldsymbol{I} \right) \cdot \boldsymbol{n}_{K,\sigma}. \tag{35}$$

The linear mapping R_s is defined in this case by following the same approach as before: Given $\boldsymbol{u}_K$ and now in addition p_K, for all cells K in $\mathcal{T}_s$, the interaction region of the vertex s, let us choose the coefficients of R_s such that the forces as defined by (35) are continuous across each subfaces, that is (14) holds, and the measure of the jumps in displacement values given by (15) is minimized. Then, we obtain at each interaction regions $\mathcal{T}_s$, the mapping $T_{s,\text{relax}}$ which corresponds to T_s in (18) for the standard MPSA method, as

$$\begin{aligned} T_{s,\text{relax}} \colon \mathbb{R}^{(d+1)N^{\mathcal{T}}_s} &\to \mathbb{R}^{dN^{\mathcal{F}}_s} \\ \{\boldsymbol{u}_K, p_K\}_{K \in \mathcal{T}_s} &\mapsto \{\boldsymbol{T}^{\sigma}_s\}_{\sigma \in \mathcal{F}_s}. \end{aligned}$$

The global system of equation is then given by the equation of conservation of momentum (20) and an equation for the pressure. The relation between the pressure and the displacement field is obtained by a discretization of the divergence operator,

$$p_K = \frac{\lambda_K}{|K|} \sum_{\{s | K \in \mathcal{T}_s\}} \sum_{\{\sigma \in \mathcal{F}_K \cap \mathcal{F}_s\}} |(K, s, \sigma)| \boldsymbol{u}^{\sigma}_{K,s} \cdot n_{K,\sigma}, \tag{36}$$

where $|\sigma_s|$ denotes the length (or surface in 3D) of the the subface γ^{σ}_s and $|K|$ the volume of the cell K. The equation (36) is a discretization of

$$\int_K p \, dx = \lambda_K \int_K \nabla \cdot u \, dx = \sum_{\sigma \in \mathcal{F}_K} \int_{\sigma} u \cdot n_{K,s} \, d\sigma$$

and defines a discrete divergence operator div_K on each cell K

$$\begin{aligned} div_K \colon \mathbb{R}^{N^{\mathcal{F}}_K} &\to \mathbb{R} \\ \left\{\boldsymbol{u}^{\sigma}_{K,s}\right\}_{s \in \mathcal{V}_K, \sigma \in \mathcal{F}_K \cap \mathcal{F}_s} &\mapsto p_K. \end{aligned}$$

Using the same arguments as in [21], one can prove that with essentially the same grid restrictions that apply for the elastic and pressure discretizations independently, the method is convergent uniformly with respect to λ. The method introduces the extra degrees of freedom p_K and it also introduces relaxation. Indeed, the divergence term in the definition of the force is imposed through p_K, that is, from the condition (36), which is imposed cell-wise. This represents a relaxation in comparison with the original MPSA method, where different values of the divergence are used for each interaction subregions (K_s

with $s \in \mathcal{V}_K$). Note that finite-volume based method for flow defines a natural divergence operator into cells and the coupling term of the mechanical system with a finite volume method, which is due to the volume changes of the cells, will also require for the mechanical system a divergence operator into cells. Hence, in the limit of incompressible fluid and small time steps, it will lead to the same constraint as the near-incompressibility constraint for the mechanical system. This means that for MPSA the ratio between the number of degrees of freedom and the near div-free condition, both defined on cells in the case of Biot's equations, is independent of the grid, while for VEM it depends on the ratio between nodes and cells. The following two MPSA methods have been implemented

MPSA:	Standard implementation, as described in Section 2.2,
MPSA-relax:	Implementation using the relaxed version where an extra pressure degree of freedom is used, see (35).

3 Numerical test cases

The test cases are designed to study the robustness of the methods with respect to grid features that are specific to subsurface applications. All of the code has been written and run using the framework of MRST, [18]. We consider only two-dimensional configurations and plan to study three-dimensional configurations in subsequent works, see [25] for 3D studies using VEM. At the moment, only full Dirichlet boundary conditions have been implemented for MPSA but the extension to other general boundary conditions such as rolling conditions (that is, component-wise Dirichlet conditions) is not difficult but requires some careful work. We summarize the different test cases in Table 2. We pay particular attention to the error in the divergence field, because of its central role in the coupling with poro-elasticity, and to the local behavior of the stress fields, due to its importance in the simulation of the development of fractures and faults.

In all test cases, we use a uniform medium. In the first test cases (Cases 1 to 4), we use the same reference solution which is computed as follows. We consider the displacement field $\boldsymbol{u} = [u_1, u_2]^T$ given by

$$u_1 = x(1-x)\sin(2\pi y) \qquad u_2 = \sin(2\pi x)\sin(2\pi y), \tag{37}$$

for x and y belonging to $[0, 1]$. Using (1), we compute the force $\boldsymbol{f}$ for which $\boldsymbol{u}$, given by (37) is the solution. In this way, we have obtained an exact solution of the linear elasticity equations (1) that we will use to compare our results in all the examples below. The boundary conditions are zero displacement on all sides. Since the problem is linear, the choice of one of the Lamé coefficient is insignificant as it only corresponds to a re-scaling of the results. Except for the simulations concerning numerical locking, we will use $\frac{\lambda}{\mu} = 1$.

Table 2 Summary of the numerical tests

Case 1	: Twisted grid
Case 2a	: Mixed grid with challenging features
Case 2b	: Large aspect ratio with hexagonal grid
Case 2c	: Large aspect ratio with triangular grid
	Two regions (Case 3)
Case 3a	: Two regions, uniform refinement (both in x and y) in one region
Case 3b	: Two regions, refinement only in the y direction in one region
Case 3c	: Two regions with the same Cartesian discretization, but with 20 extra nodes in each face at the interface
	Thin layer (Case 4)
Case 4a	: Vertical thin layer, no refinement inside the layer
Case 4b	: Vertical thin layer with refinement inside the layer, Cartesian grid
Case 4c	: Vertical thin layer with refinement inside the layer, twisted grid
	Locking examples (Case 5)
Case 5a	: $\nu = 0.495$ with hexagonal grid
Case 5b	: $\nu = 0.495$ with triangular grid
Case 5c	: $\nu = 0.495$ with quadrilateral grid
	Biot system (Case 6)
Case 6a	: Biot test case with triangle grid
Case 6b	: Biot test case with hexagonal grid

3.1 Case 1: Twisted grid with random perturbation

In this test case, we check the convergence properties of both methods. The VE method is in general first order convergent, as shown in [4, 5], but numerical tests show second order convergence under general conditions [4, 10]. For the VE method used in the near-incompressible case, see Section 3.5, where pressure is considered as an independent variable, then the pressure converges at first order, see [5, theorem 9.1]. Convergence estimates for the MPSA method are not available in the established literature but numerical tests show the same features as VEM, see [21]. Accordingly, Figure 3 shows convergence rates of two and one for the displacement and the divergence, respectively. The most refined grid is obtained by refining 16 times the initial grid. The grids which are considered in this test case are *non-regular quadrilateral* grids, see Fig-

ure 4 for an example. To generate such grids, the starting point is a uniform Cartesian grid with a given refinement. Then, a deformation field which is independent of the refinement factor is applied to each node. The deformation should leave the boundaries unchanged so that, as we apply the same boundary conditions, the exact solution is also unchanged. Such refinement setting leads however to the generation of cells that are close to parallelogram for small refinement, meaning that the grid is strongly regularized in the refinement process. Such regularity for the grid cannot be expected in a realistic context and that is why we add a random perturbation to each node. To cancel out the random part in the generation of the grids, we have produced the same error plots several times and we observe that the convergence rates keep the same characteristics. Let us briefly explain how the discrete L^2 and L^∞ norms are computed for both methods. The displacement values are defined on nodes for VEM and at cell centers for MPSA, so that the discrete L^∞ norms for the displacement, even if not equivalent, provide comparable estimates. For both methods, the divergence is defined on cells, so that the discrete L^2 and L^∞ norms are directly comparable. The stress is piecewise constant for VEM, while MPSA defines forces on faces. We define the discrete L^2-norm for stress for the MPSA method as the summation of the discrete L^2 norms of the force over the edges. In this way, we obtain an averaged quantity but it is not directly comparable with the discrete L^2 norm used for stress in VEM, which is the standard volume integral over the domain.

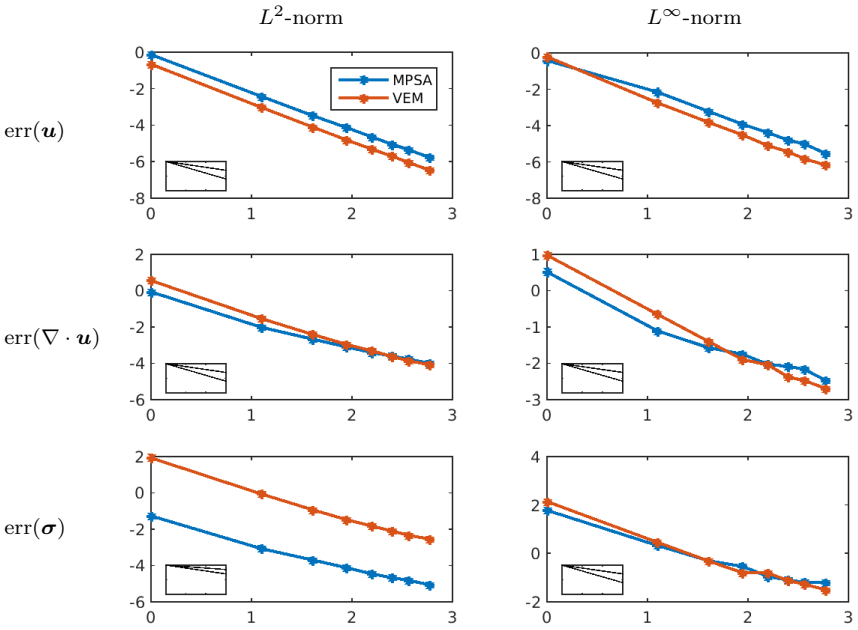

Fig. 3 Convergence plot for a twisted Cartesian grid. The L^2-norm (left) and L^∞-norm (right) of the error are plotted for the displacement (upper row), the divergence (middle row) and the stress (lower row). Logarithmic scales are used and the values on the x-axis give the logarithms of the refinement factor, which we denote N. In the small boxes, the slopes corresponding to a convergence factor of one and two are represented (by definition, a convergence factor of r corresponds to an error decaying as err $= (1/N)^r$).

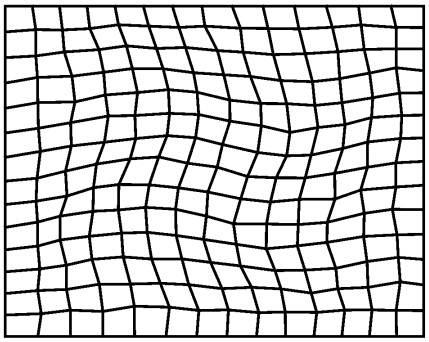

Fig. 4 Example of a deformed grid, with refinement factor equal to 7. The grid is obtained from a Cartesian grid by applying a smooth given deformation field to the nodes, which also leaves the boundary invariant. In addition, random shifts are added to avoid a regularization of the grid as the refinement is increased, see the explanations given in the text.

3.2 Case 2: Mixed cell types

We set up a case (Case 2a) with a grid that combines several difficulties. The grid is made up by, first, assembling regions with different cell types (triangles, quadrilaterals, hexahedral) and, then, twisting the grid. Many cells have unfavorable aspect-ratio. There are also hanging nodes. However, as it can be seen from Figures 5, 6 and 7, the methods manage to capture rather well the exact solution. Note that MPSA has problem to handle triangles where not all the angles are smaller than 90 degrees. Nevertheless, the error that occurs at these cells does not spread to the whole domain.

We investigate further the case of large aspect ratio for hexagonal (Case 2b) and triangular grid (Case 2c). Both grids are obtained by stretching uniform grids in the x-direction with a given factor. In both cases, we use an aspect ratio of 7. In Figure 8 and 9, we observe that the VEM method manages to handle the hexagonal case correctly while, for the grid made by triangles, it produces a displacement field that captures the correct trend but fails quantitatively and oscillatory values for the divergence. By construction, VEM methods are always well-posed in the sense that a solution to the discrete system always exists. However, the quality of the solution may be very poor. The situation of very large aspect ratio has been analyzed in more details in [24], where it is shown to depend on the choice of the stabilization term. In contrast, All MPSA and MPFA methods require a local coercivity condition for well-posedness. This condition is implicitly defined, in that it depends on a combination of material heterogeneity, anisotropy and grid geometry. In Figure 8, the poor quality of the results for the MPSA method can be measured by comparing them to the results of VEM, which can be considered here as a reference solution. The poor performance of MPSA is caused by the deterioration of the grid with respect to the criteria mentioned above, which enter in the well-posedness condition. For the triangle case, the MPSA method simply fails and the results are not shown. Note that we can also make the method fail for the hexagonal case by considering sufficiently high aspect ratio. For MPFA, well-posedness conditions have been made explicit in [13, 14] in the case of quadrilateral grids, by reformulating the MPFA method as a Mixed Finite Element (MFE) method where quadrature rules, instead of exact integration, are used in the assembly. In [2], the authors reformulate the MPFA-O method for general grids using a discrete functional framework. Then, they are able to derive a sufficient well-posedness condition for the method in form of *local* (defined at each node) coercivity conditions. Well-posedness conditions of the same type have been derived for MPSA in [22]. However, as we just mentioned, those conditions are defined implicitly and do not lend themselves to simple expressions. Note that a more restrictive, but also more tractable, well-posedness condition on each cell is also proposed in [2] for MPFA. The new MPSA method presented in [12] overcomes many of the limitations we observe for triangular grids that are observed in case 2c.

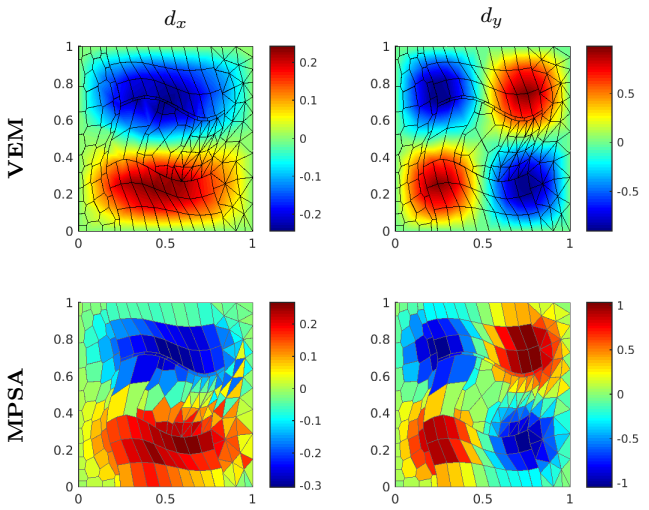

Fig. 5 Displacement field $\boldsymbol{u}$ (Case 2a) for the MPSA and VE methods. Even for this grid that was artificially set up to mix different challenging cell types, both methods produce satisfactory results

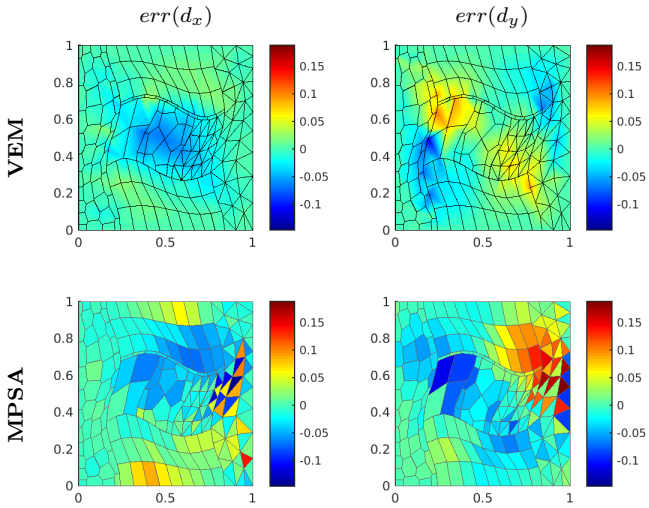

Fig. 6 Error in t he displacement field $\boldsymbol{u}$ for both methods (Case 2a). The error is slightly higher for the MPSA method compared to VEM but not in a significant way.

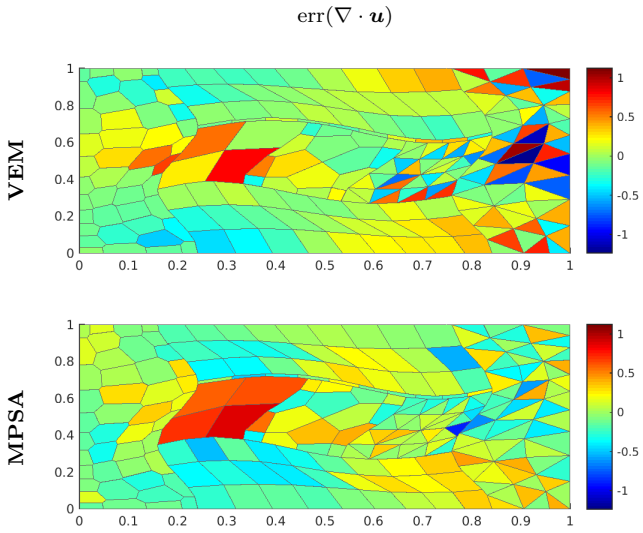

Fig. 7 Error in the divergence field $\nabla \cdot \boldsymbol{u}$ for both methods (Case 2a).

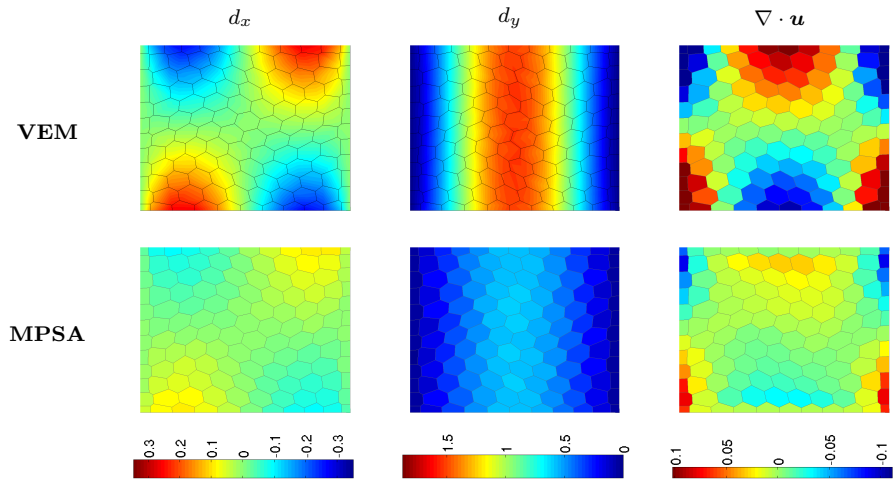

Fig. 8 Aspect ratio 7 using an hexagonal grids (Case 2b). For the purpose of a better visualization, we plot the values of the displacement and divergence fields on a grid which is stretched back to a uniform grid (with aspect ratio 1). The VEM is able to produce reliable results in this case. The MPSA method, as the MPFA method, has inherent limitations which makes it unsuitable for grids with high aspect ratio, as the plots from the last row can confirm.

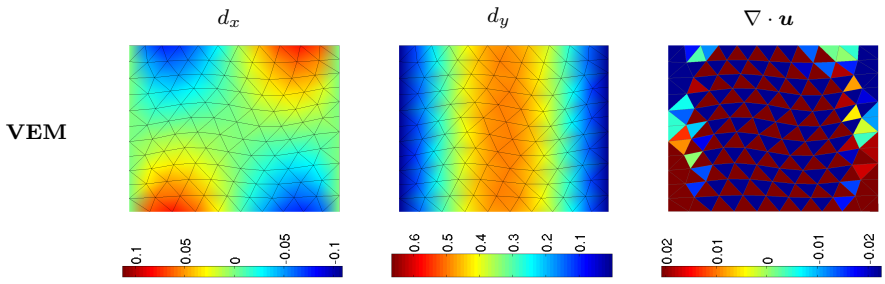

Fig. 9 Aspect ratio 7 using a triangular grid (Case 2c). The same visualization procedure as in Figure 8 is used here. The VEM method leads always to a well-posed system of discrete equations but the quality of the approximation is affected by high aspect ratio in this case. The solution for the displacement field is captured qualitatively but not quantitatively (compare with Figure 8). The solution for the divergence presents oscillations.

3.3 Case 3: Stability with respect to decomposition of the grid in regions with different refinement

Grids in subsurface simulations are typically heterogeneous, mixing cells of different sizes and shapes. We consider two test cases where two regions of equal size but with different refinements are set side by side. For the first case (Case 3a), the refinement in the region on the right-hand side is isotropic in the sense that it is done in both x and y direction. For the second case (Case 3b), the grid on the right hand-side is refined by splitting the cells only in the y direction. In both cases, we keep the same coarse domain on the left-hand side. See Figure 10

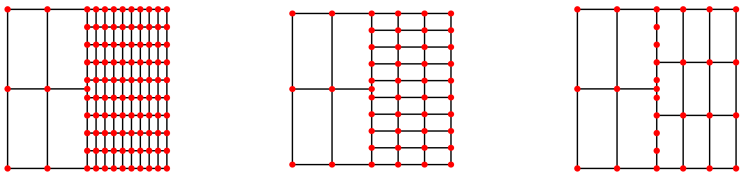

Case 3a Case 3b Case 3c

Fig. 10 Illustration of the grids used in case 3. The nodes are plotted in red and, for illustration purpose, we use a low refinement. We set also the nodes of the two regions so that they do not coincide, except at the boundaries. In this way, we avoid artificial correlations between the node locations as we increase the refinement.

In Figure 11, we look at the error when the refinement factor on the right-hand side is increased in both directions. By refinement factor, we mean the number of sub-intervals that an edge of the initial grid is divided into to obtain the refined grid. We observe that the error for the VE method increases significantly for the divergence of the displacement and the stress in the L^∞-norm. In the L^2-norm, the increase is much less severe, which indicates that error is essentially of local nature. This is confirmed by the plots of Figure 12. In Figure 13, we plot the force at the interface between the two regions. For the VE method, the stress is defined inside the cells so that we obtain two curves at the interfaces, one for the coarse cells, the other for the fine cells. The force is computed at a cell interface by integrating the product of the stress in the cell with the normal of the interface. For the MPSA method, the force is defined on the edges and is therefore readily available at the interface. We observe that the stress for the VE method is strongly oscillating in the cells which belong to the refined region. For the horizontal component of the force, the oscillations take the form of peaks, while the force computed from the cells belonging to the coarse region is smooth and rather close to the analytical value which is zero due to the symmetry of the problem. For the y-component of the force, the analytical value is no longer constant. For the VE method, the value computed from the cells of the fine region still presents

oscillation but, in addition, the value computed from the coarse region presents strong variations, approximating the smooth analytical values by a staircase function. Such behavior may be problematic if the solver is coupled with a fracture model, typically non-linear, based on local value of the stress field. In comparison, the MPSA method yields much smoother approximations. In Figure 14, we plot the error in displacement at the interfaces. From this figure, it is clear that the computed solution present artificial discontinuities between the nodes belonging to the two different regions, see also Figure 12. In case 3c, we study further this numerical artifact.

Let us now consider the case where the refinement is done only in the y-direction (Case 3b). The discretization at the interface is the same as in the previous case but the cells at the right-hand side get a relatively larger area and a larger aspect ratio. In Figure 15, we observe that the error in the L^∞-norm no longer grows for the VE method. The strong oscillations in the x-component of the force are smaller compared to the previous case, as we can observe by comparing Figures 13 and 16. We have checked that the same type of discontinuities as shown in 14 is also observed in this case. The distribution of the errors for the displacement and divergence fields is also similar to the one that are obtained in the previous case (Case 3a) and shown in Figure 12.

Finally, we setup a case where the two regions have the same coarse mesh but we add extra nodes at the interface (Case 3c). In this way, we remove the difference in volumetric refinement between the two regions and isolate the effect of edge refinements. In Figure 17, we plot the error displacement for the VE method at the interface and observe that the hanging nodes and the nodes that belong to horizontal edges behave differently. This case shows that the error at nodes observed in the previous cases is not due to the volumetric refinement but to the edge refinement, on one side of the grid. We propose the following explanation for this behavior. In the VE method, the basis elements are not computed, only the degrees of freedom are used for the assembly and linear approximations remain exact but, in the case of elements with many nodes, the basis elements will be highly non-linear. We illustrate this in Figure 18 where we compute some of the virtual basis elements. To define the virtual elements in the cells (that is, make in them no longer virtual), we use *harmonic lifting* as in [10], see also [6]. We consider the same type of cells as the ones which lie at the interface in Case 3c, reducing the refinement to ten nodes in order to make the pictures easier to read. For simplicity, this illustration has been created using the Laplace operator and not the linear elasticity operator. We can sort the virtual basis in three categories:: Basis with two large edges (type I), basis with a large and a small edge (type II), basis with two small edges (type II), see Figure 18. The virtual basis elements have very sharp gradients in small regions and are almost flat elsewhere so that most of their energy is concentrated in high frequencies. In this case, the projection operator $\mathcal{P}$ over linear function, see section 2.1, does not provide a good approximation and most of the contribution for this basis element will be handled by the regularization term, s_K, which is only a poor substitute for a_K. We have computed the fraction of the energy that comes from the

orthogonal part of the projection, for the three types of basis functions,

$$\frac{a_K(\phi - \mathcal{P}\phi, \phi - \mathcal{P}\phi)}{a_K(\phi, \phi)} = \begin{cases} 0.49 & \text{if } \phi \text{ is of type I,} \\ 0.90 & \text{if } \phi \text{ is of type II,} \\ 0.99 & \text{if } \phi \text{ is of type III.} \end{cases} \tag{38}$$

Since in this case the length of the large and small edges are $L = 1$ and $l = 0.1$, respectively, these computations confirm the following orders of magnitude,

$$\frac{a_K(\mathcal{P}\phi, \mathcal{P}\phi)}{a_K(\phi, \phi)} \approx \begin{cases} 1 & \text{if } \phi \text{ is of type I,} \\ l/L & \text{if } \phi \text{ is of type II,} \\ (l/L)^2 & \text{if } \phi \text{ is of type III,} \end{cases}$$

which can be obtained by roughly estimating the area of the support of the gradient of the basis function. In Figure 14, we observe that, at the interface region, the displacement values obtained at nodes that are connected to a large edge (left region) have different errors to those connected to a small edge (right region).

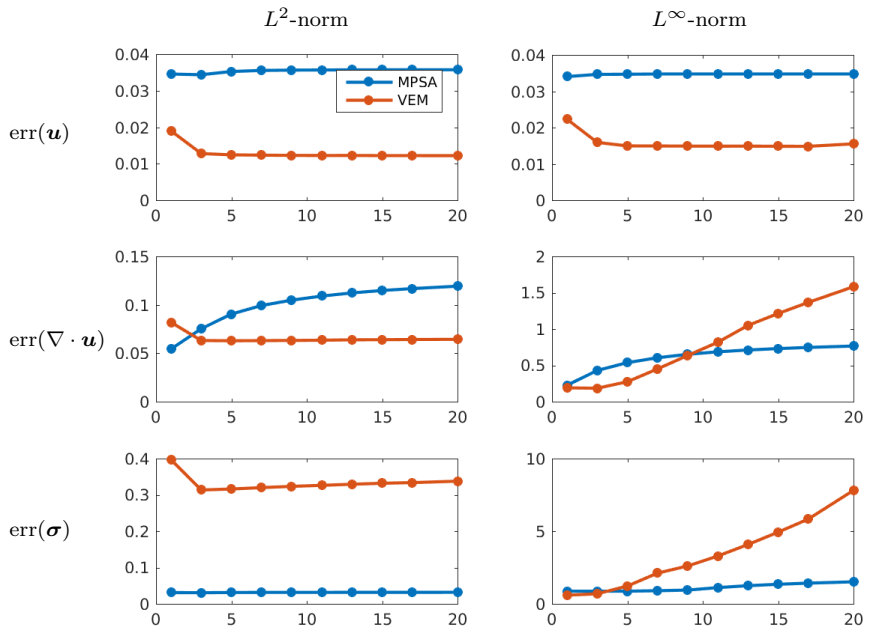

Fig. 11 The region at the right-hand side is refined equally in both the x and y direction (Case 3a). The L^2-norm (left) and L^∞-norm (right) of the error are plotted for the displacement (upper row), the stress (middle row) and the divergence (lower row). The x-axis indicates the refinement factor in the right-hand side region. We can see that both methods are robust with respect to the increase of heterogeneity that is introduced by an asymmetric refinement. The increasing error in the L^∞ norm for the VEM method shows that the error is more localized for this method.

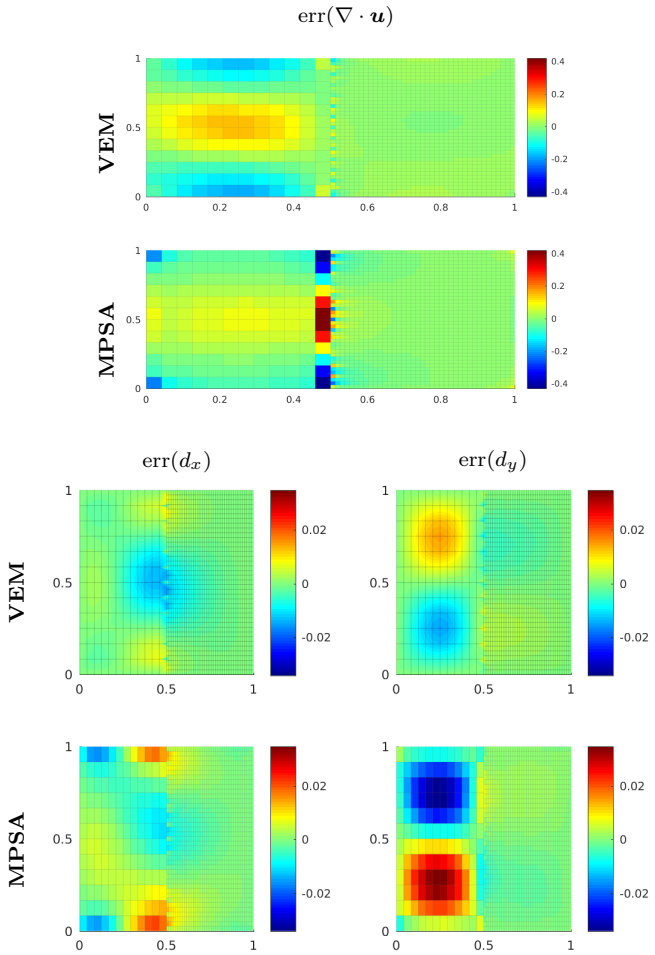

Fig. 12 Plot of the error in the divergence and in the horizontal and vertical displacement, for Case 3a. The vertical refinement ratio in the region on the right-hand side is equal to 20. We can observe how the error is more localized around the interface between the two regions for the VEM method compared to MPSA. As far as the divergence field is concerned, we observe how the MPSA method spreads the error to the large cells of the left-region at the interface.

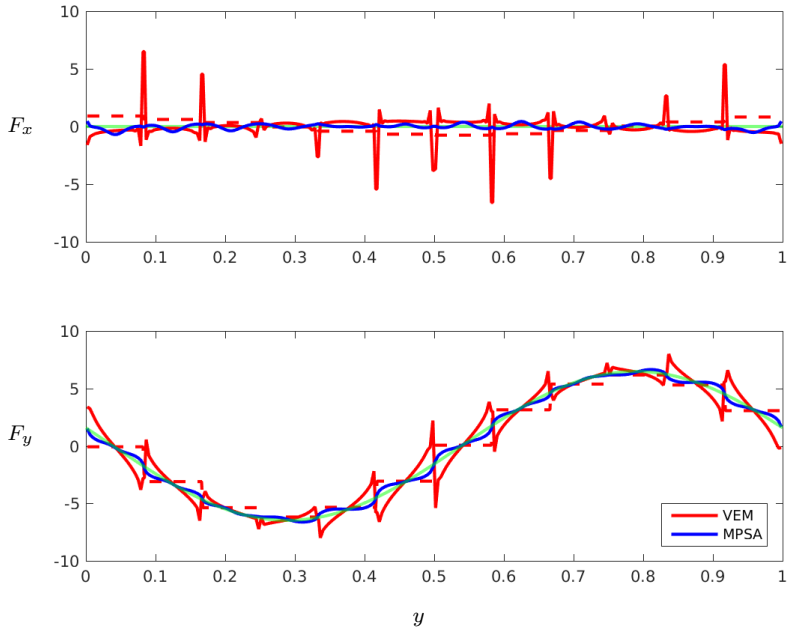

Fig. 13 Plot of the forces at the interface between the two regions for Case 3a. For the MPSA, the stress at the interface is directly available. For the VE method, the stress is computed in the cells so that there are two values, one from the coarse and the other from the fine region, which can be used to define the value of the stress at the interface. We observe that VEM produces oscillations in the stress that do not appear with MPSA.

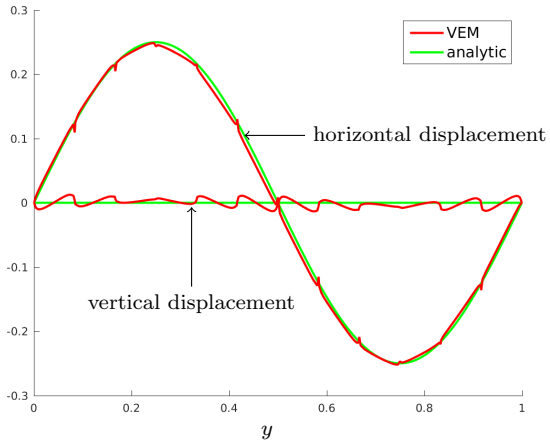

Fig. 14 Plot of the displacement for the VE method (Case 3a). We can observe two different responses at the interface, in form of peaks in the horizontal displacement and jumps in the vertical displacement. The locations of the peaks and jumps correspond to the nodes that belong to the coarse region. See also Figure 17 for a related experiment.

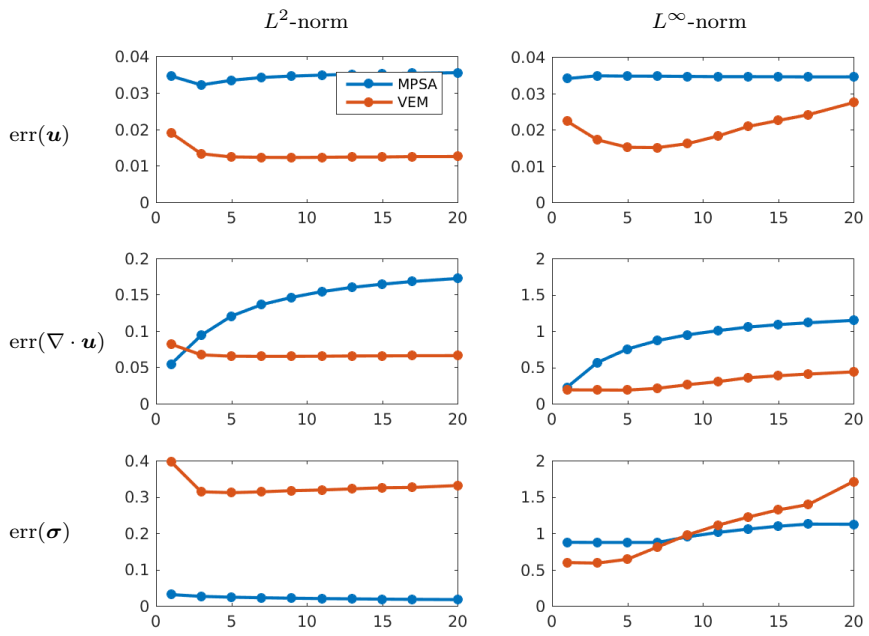

Fig. 15 The region at the right-hand side is refined only in the y direction (Case 3b). The L^2-norm (left) and L^∞-norm (right) of the error are plotted for the displacement (upper row), the stress (middle row) and the divergence (lower row). The x-axis indicates the refinement factor in the right-hand side region. We can see that, also in this case, the methods are robust with respect to asymmetric refinement.

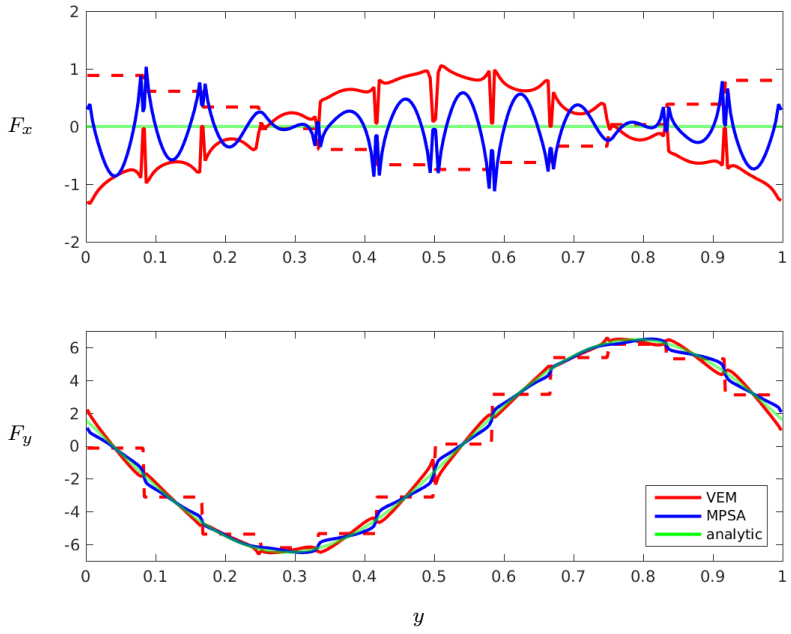

Fig. 16 Plot of the forces at the interface, for Case 3b. The values are obtained in the same way as in the plot of Figure 13. The magnitude of the oscillations is lower for VEM compared to the previous case (Case 3a).

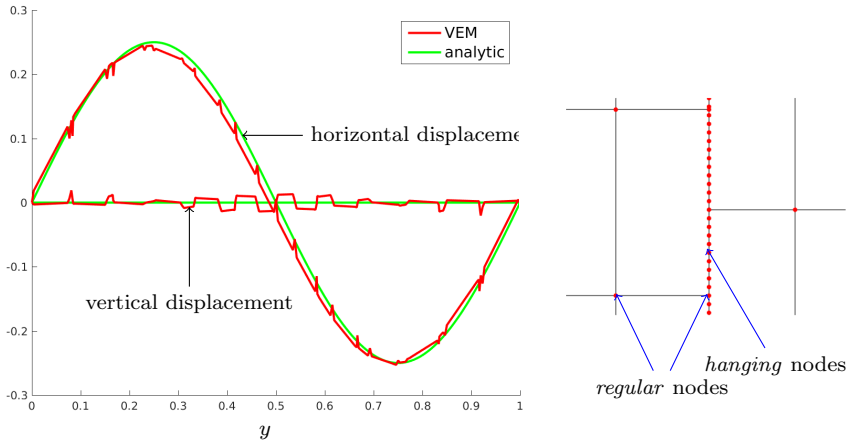

Fig. 17 On the left, plot of the error in displacement at the interface, only for the VE method in the case where there is no layer but 20 extra nodes on each face at the interface (Case 3c). On the right, we plot a sample of the grid used for this experiment where the nodes are plotted in red. From this experiment, we can infer that the different response between the nodes (hanging versus regular nodes) is not due to volumetric refinement, which was present in the previous cases (Cases 3a and 3b)

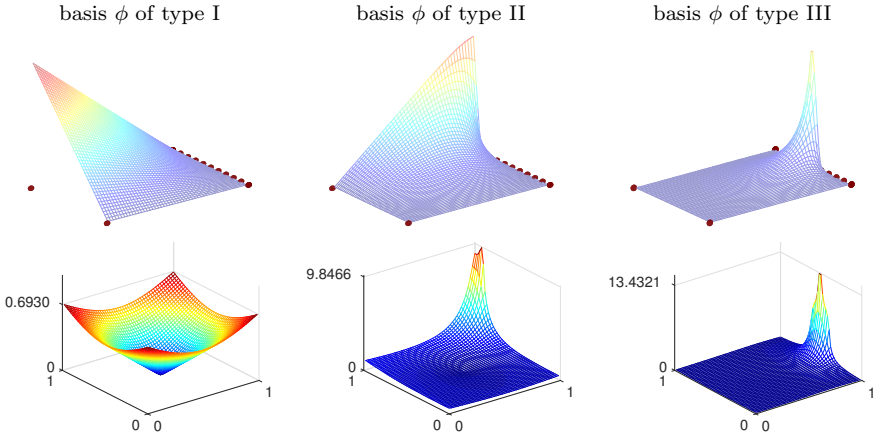

Fig. 18 Illustration for Case 3c using the Laplace operator. First row: Plot of three virtual basis elements for a square cell with 10 edges on one side. The red dots indicates the position of the nodes. We can sort the virtual basis in three types: Basis with two large edges (left), basis with a large and a small edge (middle), basis with two small edges (right). Second row: Plot of the norm of the residual of the projection, that is $|\nabla(\phi - \mathcal{P}\phi)|^2$, for the basis function represented above. The basis of type III contains much more *residual* energy than the basis of type II and type I, see (38).

3.4 Case 4: Layer between two domains

In subsurface flow, significant parts of the flow are concentrated in the fractures of the rock. We set up therefore test cases that reproduce the geometry of a fracture by introducing a thin layer in an otherwise uniform Cartesian grid. If this layer were a fracture or a damaged zone, then it would have very different mechanical properties than the rest of the matrix, but, in our test case, the layer is assigned the same properties as the rest of the domain so that the analytical solution given by (37) still holds. In this way, we isolate the errors of the numerical methods that are induced by a typical geometrical discrete representation of a fracture, without including the mechanical effects of the fracture itself. First, we consider a test case (Case 4a), where the layer is discretized with the same level of refinement in the y direction as the rest of the matrix. In Figure 19, we plot the error as we let the width of the layer get thinner and thinner. We observe that the error does not grow, indicating the robustness of both methods with respect to the thickness of the layer. Figure 20 gives the error in displacement and divergence of displacement. We observe that the error in displacement is more localized for the VE method and more spread for the MPSA method, which is consistent with the results of Figure 19 when comparing the L^∞ norm and L^2-norms. In Figure 21, we present a plot of the forces at the interface between the layer and the region with coarse cells. We choose the left interface of the layer but the results on the other interface have the same characteristics. We observe that the MPSA method gives slightly but not significantly better approximation of the force.

In applications, the discretization level of the fracture layer may typically not match the one of the matrix. We investigate this situation by setting up a test case where the refinement in the layer is increased (Case 4b). We also consider the same case but we twist the grid (Case 4c) to break eventual symmetry effects. In Figure 22, we can observe the L^∞-norm of the error for the stress grows significantly for the VE methods. The error in divergence remains zero in the Cartesian case (Case 4b) but, by looking at the twisted case (Case 4c), we conclude that this is only due to a symmetry effect. The error in displacement for this test case is plotted in Figure 23 which also serves as an illustration of the twisted grid we are considering in Case 4c. We observe also the type of oscillations for the VE method as previously in the case of two adjacent regions with different discretization levels (namely Case 3a). Also in this case, the MPSA method gives a smoother approximation closer to the analytical solution. In Figure 24, we present a plot of the divergence along the interface together with a zoom on the region around of the error in divergence. Note that for the MPSA method, we use the finite volume definition of the divergence, that is, the value of the divergence in the cell is equal the sum of the normal component for each face. Again, we observe how the error in the VE method remains highly localized and concentrates inside the layer while the error for the MPSA methods spreads more to the coarse cell.

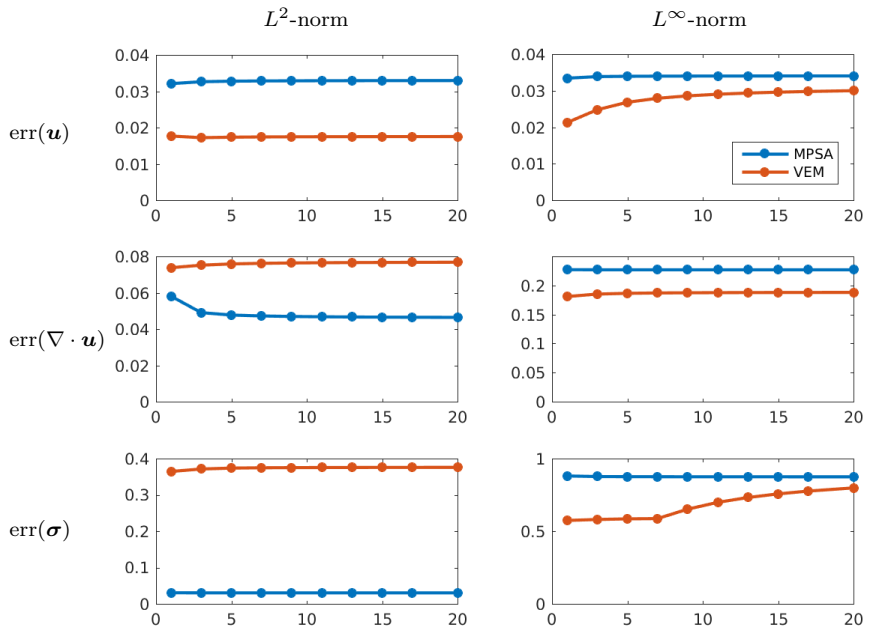

Fig. 19 The width of the layer is decreased and no vertical refinement in the layer is used (Case 4a). The L^2-norm (left) and L^∞-norm (right) of the error are plotted for the displacement (upper row), the stress (middle row) and the divergence (lower row). The x-axis indicates the reduction factor for the width of the layer. We observe that the methods are robust with respect to layer refinement.

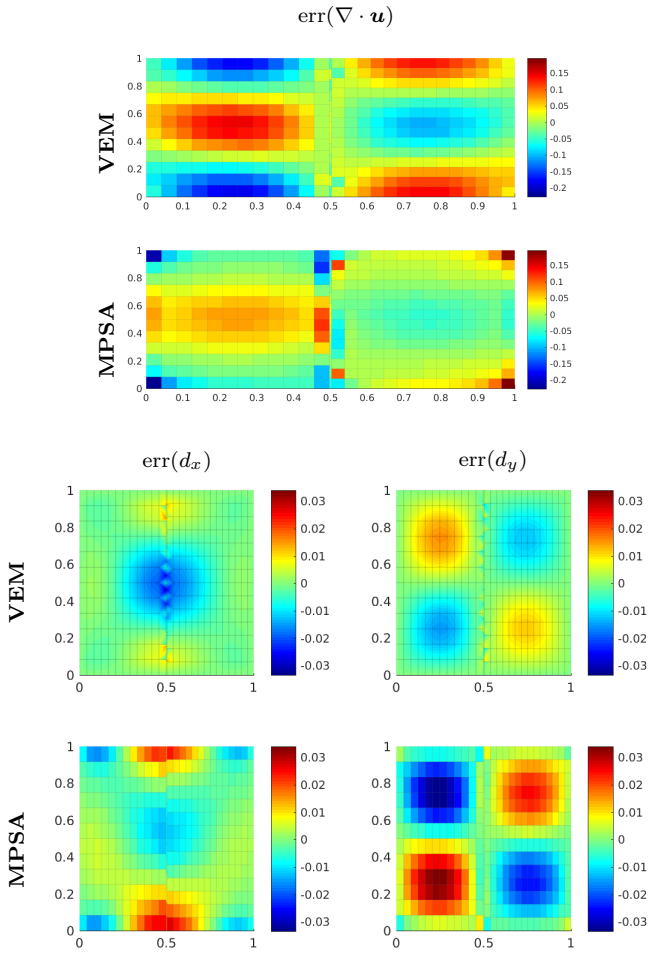

Fig. 20 Error in the divergence (two upper figures) and the displacement in both x and y directions (Case 4a). The width of the layer is 20 times smaller than the adjacent cells. We observe that the error is more local and concentrated at the interface for the VEM while it spreads throughout the domain for MPSA. For the divergence field, we observe the same spreading of the error to the large cells in the coarse region for the MPSA method, as in Case 3, see Figure 12

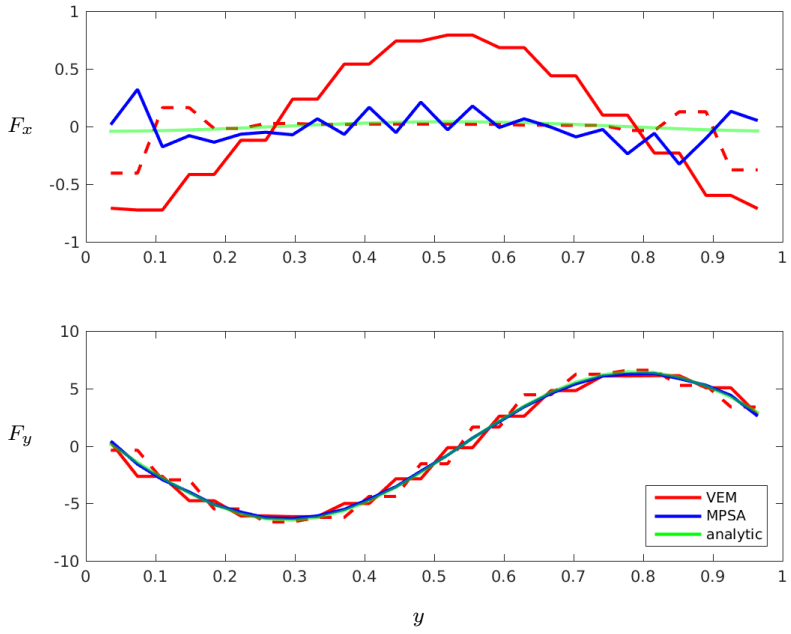

Fig. 21 Plot of the forces at the interface, for Case 4a. The values are obtained in the same way as in the plot of Figure 13. The conclusions are similar to the two region cases (Case 3) in the sense that we observe more oscillations for VEM than for MPSA.

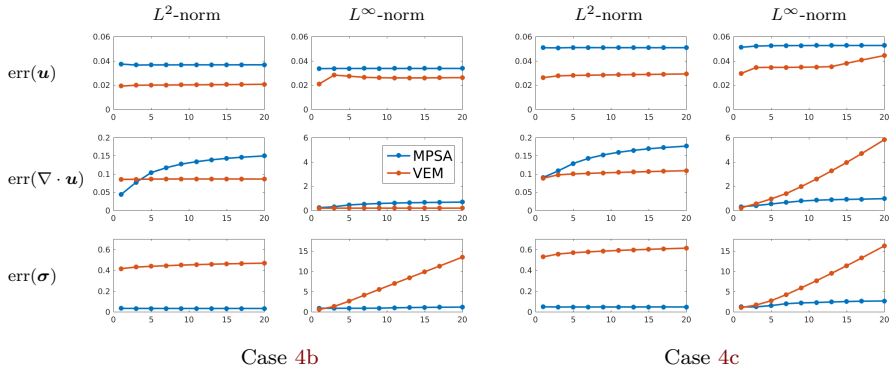

Fig. 22 The width of the layer is decreased but the aspect ratio of the cells in the layer is preserved. The L^2-norm (left columns) and L^∞-norm (right columns) of the error are plotted for the displacement (upper row), the stress (middle row) and the divergence (lower row). On the left, we have the Cartesian case (Case 4b) and the twisted case on the right (Case 4c). In all plots, the x-axis indicates the value of the reduction factor of the layer width. The relatively low error in the L^∞ norm of the divergence field in case 4b is in fact only due to symmetry effects, as it can be seen by comparing with case 4c.

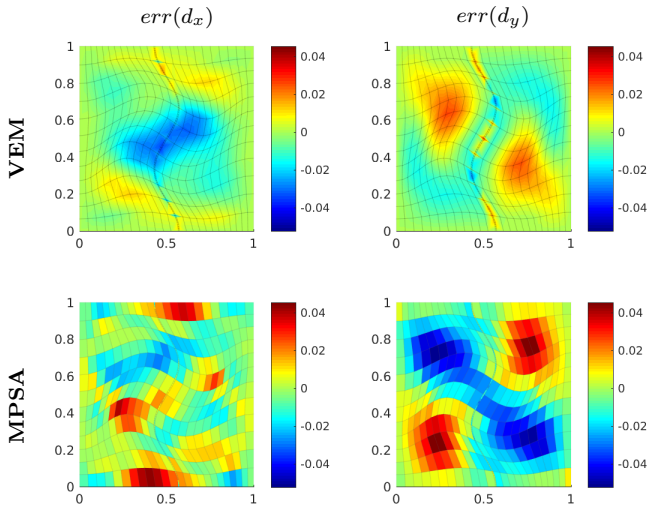

Fig. 23 Plot of the error of the displacement in x and y directions (Case 4c). We can observe, even more clearly than in Figure 20, how the error for the VEM method is concentrated in the layer while it spreads out in for MPSA.

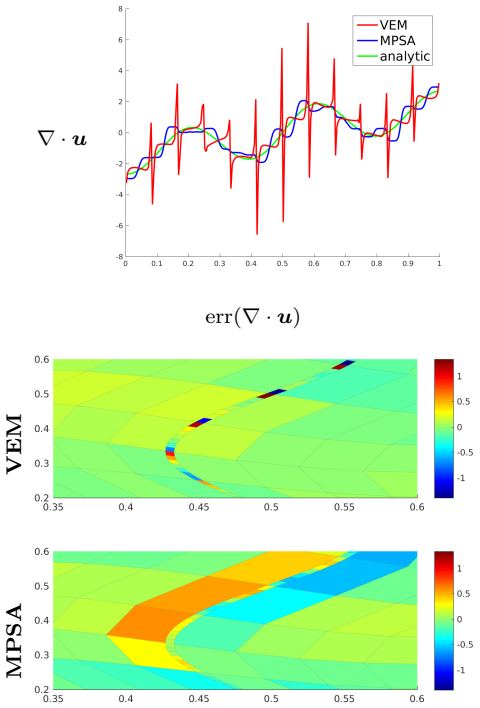

Fig. 24 Plot of the divergence at the interface of the layer for Case 4c (top). We observe large oscillations for the VE method (middle) inside the layer but they remain confined in the layer. Comparatively, the oscillations are weaker for MPSA (bottom) but the error spreads more to the neighboring cells.

3.5 Case 5: Stability near incompressibility

In the following experiments, we set up cases to study the behavior of the methods with respect to the near-incompressibility limit. The boundary conditions are zero displacement on the left and right side and free displacement on the top and bottom sides. The external force is a constant volumetric vertical force, like for example a gravitational force. We present test results for three grid types which highlights the main features. We consider grids made of hexahedrons (Case 5a), triangles (Case 5b) and quadrilaterals (Case 5c). To generate each grid, we start with a uniform tessellation. Then, the grid is twisted in order to remove any side-effects that may arise from symmetry. The resulting grids can be seen from Figure 25, 26 and 27. In the case of hexahedrons (Figure 25), we observe numerical locking for VEM and MPSA while VEM-relax, VEM-relax-extra and MPSA-relax give a good approximation of the solution, see Section 2.3.3 for the definitions of these methods. The numerical locking for VEM can be observed directly in the displacement field. Indeed, the amplitude of the computed displacement is much smaller than the one of the exact solution, so that the material appears to be stiffer than it actually is, hence the name of *locking* which is used to denote this numerical artifact. The numerical locking for MPSA is more visible in the divergence field, as artificial oscillations. Note that we could have chosen the parameter ν closer to 0.5 where the effects of numerical locking lead to a computed solution which is far off the exact solution, but we prefered to show examples where we can still recognize the solution and observe the beginning of the perturbations caused by locking. We summarize all the results in the table 3.

	VEM	VEM relax	VEM relax extra	MPSA	MPSA relax
hexagonal	NL	OK	OK	NL	OK
triangle	NL	NL	OK	OK	OK
quadrilateral	NL	NL	OK	OK	OK

Table 3 Overview of the results for numerical locking experiments, where NL stands for numerical locking and OK for free of numerical locking. Numerical locking depends on the combination of the grid and the method. We observe an overall better resilience of MPSA with respect to numerical locking.

For the VEM method, numerical locking occurs always if we do not use the *Stokes relaxation* with the standard regularization term. The *Stokes relaxation* (VEM-relax) corresponds to introducing an extra cell degree of freedom corresponding to the solid pressure $\lambda \nabla \cdot \boldsymbol{u}$. In VEM, this can be seen as introducing a modified regularization term since the solid pressure can be locally eliminated. Once the relaxation is done, the results we obtain are in accordance with the theory, as presented for the Stokes problem in [5, Section 8]. In the

case where a node belongs to more than three edges, as for the triangle or quadrilateral grid, *bubble-edge* degrees of freedom have to be included. Such degrees of freedom are obtained by adding an extra node on some of the edges. The requirement on the final grid is that each node can be connected to at most three edges that do not have bubble-edge element. In VEM-relax-extra, by adding nodes on every edge, we always fulfill this requirement and, as expected, no numerical locking is observed. In the hexagonal case, each node belongs to only three edges, so that the stability of the method is guaranteed. In comparison to VEM, the MPSA method behaves surprisingly well. Indeed, in two of three cases, for quadrilateral and triangle grid, the method does not show any sign of numerical locking in our experiments. The counting argument, presented in section 2.3.2, which consists of comparing the number of degree of freedom and the number of *near* constraint, predicts opposite behavior for the MPSA and VEM methods, as the methods operate with degrees of freedom that are dual to each other (dual in the sense of dual grid). Our conclusion there was that the hexagonal grid is favorable and the triangle grid unfavorable for VEM, and the opposite conclusion for MPSA. However, this argument applies at different levels of grid enrichment for VEM and MPSA. For VEM, numerical locking occurs on all of the original grids (hexagonal, quadrilateral, triangular) and the favorable hexagonal grid becomes free from numerical locking only after introducing pressure cell degrees of freedom (Stokes relaxation) or equivalently modify the regularization term. For MPSA, two of the original grids (quadrilateral and triangle) are free from locking *without* further enrichment. Only the unfavorable hexagonal grid presents locking, which is removed by the Stokes relaxation. Further enrichment of the grid is not necessary to get rid of locking, as it was the case for VEM. This result is interesting for applications to the Biot equation. Indeed, if a MPFA method is used for the flow to compute the fluid pressure, all the necessary operators are then already introduced to deal with the solid pressure and no numerical locking is then expected to appear with this formulation.

We also note that the solution obtained from MPSA-relax contains slightly more oscillations and is not as good as the one obtained by standard MPSA. This result highlights the relaxation effect of the method, which means that, if numerical locking is not an issue, the standard MPSA is expected to give less error than MPSA-relax. In the setting of VEM, it corresponds to the fact that, when there is no locking, VEM has in general a smaller error constant than VEM-relax, as the latter considers a less accurate approximation of the divergence, see (27) compared to (25).

Finally, we illustrate the artifacts that are introduced by numerical locking in solutions to the poro-elastic Biot's equation. We use a test case inspired from [11] where the authors study similar effects. We consider a two dimensional domain with three regions of equal area and where the region in the middle has a permeability that is 1×10^{-5} smaller than in the two other regions, see top of Figure 28. The boundary condition are no flow on the sides and at the bottom for the flow and, for the solid part, we impose no displacement at the bottom and no horizontal displacement with free vertical displacement on the

sides. We assume that the water is incompressible, that is $c_0 = 0$ in (22), and the other parameters are $\mu = 1$, $\lambda = 1$ $\Delta t = 0.1$ $\alpha = 1$ (in SI units). The system is initially at rest (displacement and pressure equal to zero) and we start the experiment by setting at the top of the domain the pressure equal to zero and apply a constant vertical force equal to one and pointing downwards. At $t = 0$, the pressure instantaneously jumps to one in the whole domain. To see that, we consider the asymptotic expansion of (22) for very small time step or, equivalently, consider the system given by (23) after letting $\Delta t = 0$. We obtain

$$\nabla \cdot \boldsymbol{\sigma} + \nabla p = 0, \tag{39a}$$

$$\nabla \cdot \boldsymbol{u} = 0. \tag{39b}$$

We recognize the Stokes system. Given the boundary conditions $\boldsymbol{\sigma}\boldsymbol{n} + p\boldsymbol{n} + \boldsymbol{f}_{ext} = 0$ for $\boldsymbol{f}_{ext} = -\boldsymbol{n}$, we can check that $p = 1$ and $\boldsymbol{\sigma} = 0$ in the whole domain Ω is a solution. Since the solution to the Stokes system is unique, this is indeed the solution. Then, since the fluid pressure is zero at the boundary, the liquid will start flowing out. In the first permeable region, for the given time step, pressure variations are sufficiently large to keep us away from the incompressibility constraint. In the second region, with very low permeability, the exact solution of the time-discretized system has a divergence of the displacement field which is highly constrained, in this case equal to some constant because the value of $\Delta t \nabla \cdot (\boldsymbol{K} \nabla p^{n+1})$ approaches zero. When the numerical scheme is not able to capture such incompressible displacement field, they are then approximated by an oscillatory divergence field (see, for example, VEM case in Figure 26). Then, the numerically computed fluid pressure will adjust to it and become oscillatory. In our experiments, we use the VEM-relax method for the mechanical part and a Two Point Flux Approximation (TPFA) to discretize the differential operators in the flow equation. We consider a triangle and an hexagonal grid and, as we have seen, numerical locking occurs for the triangle grid while it does not affect the hexagonal one, see 3. In Figure 28, we observe as expected that oscillations in the fluid pressure appear in the case of the triangle grid while the hexagonal grid manages to reproduce a reliable pressure field.

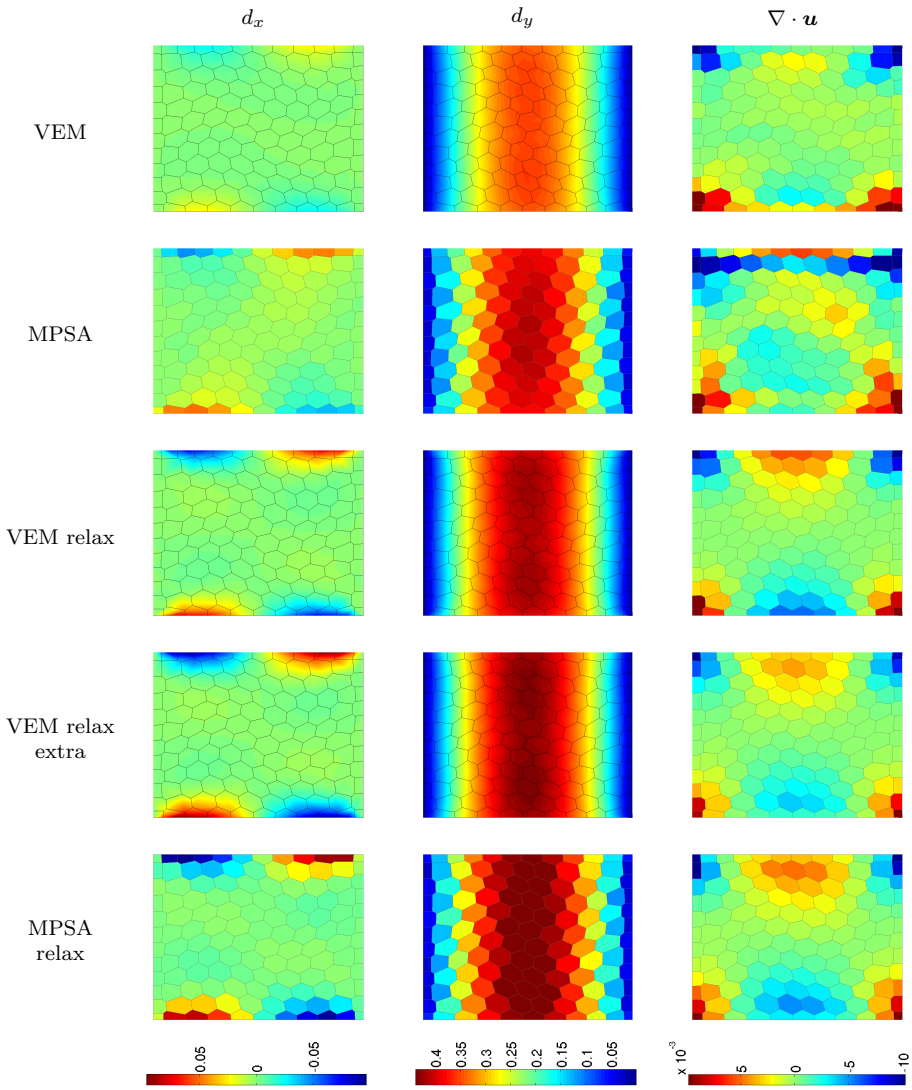

Fig. 25 Hexagonal grid and $\nu = 0.495$ (Case 5a). MPSA and VEM suffers from numerical locking. VEM-relax, VEM-relax-extra and MPSA-relax are free from numerical locking. The numerical locking is easiest observed from the divergence field which becomes oscillatory but it can also be observed in the low amplitude of the displacement field (hence, the name of *locking*).

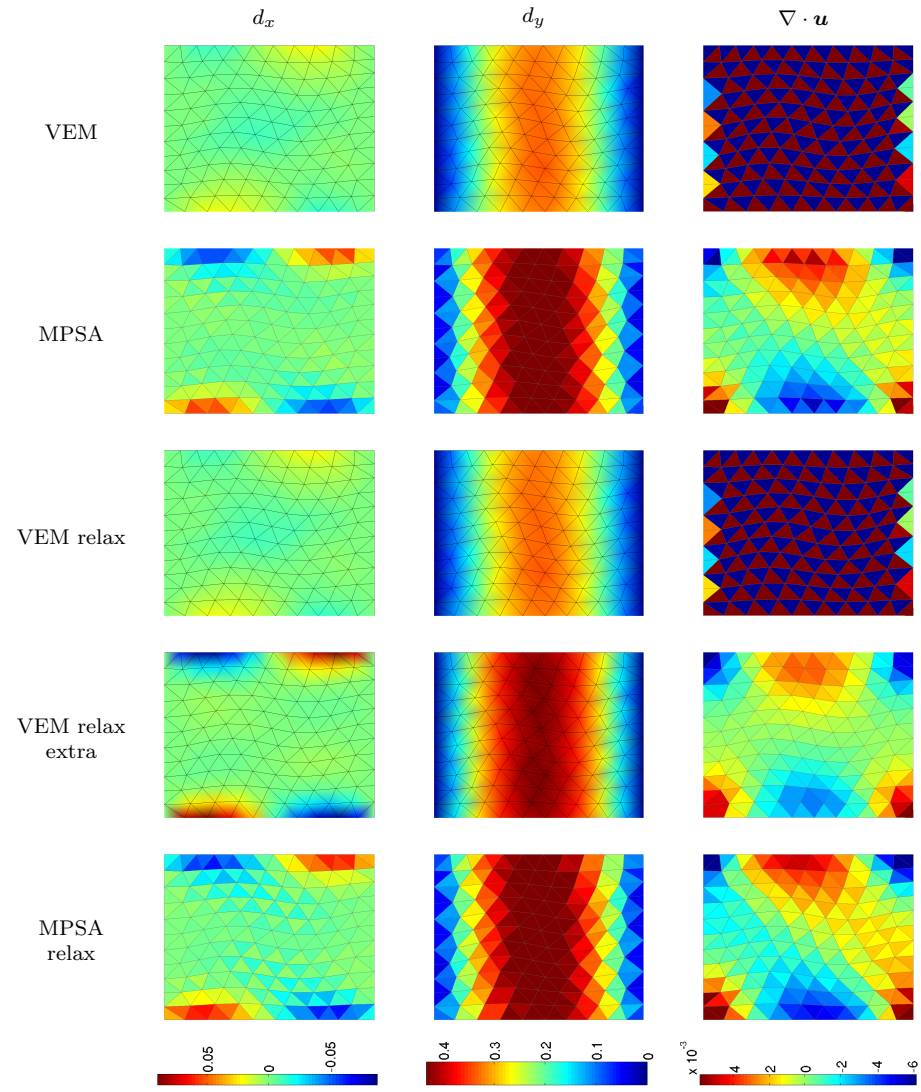

Fig. 26 Triangular grid and $\nu = 0.495$ (Case 5b). VEM and VEM-relax suffers from numerical locking. MPSA, MPSA-relax and VEM-relax-extra are free from numerical locking.

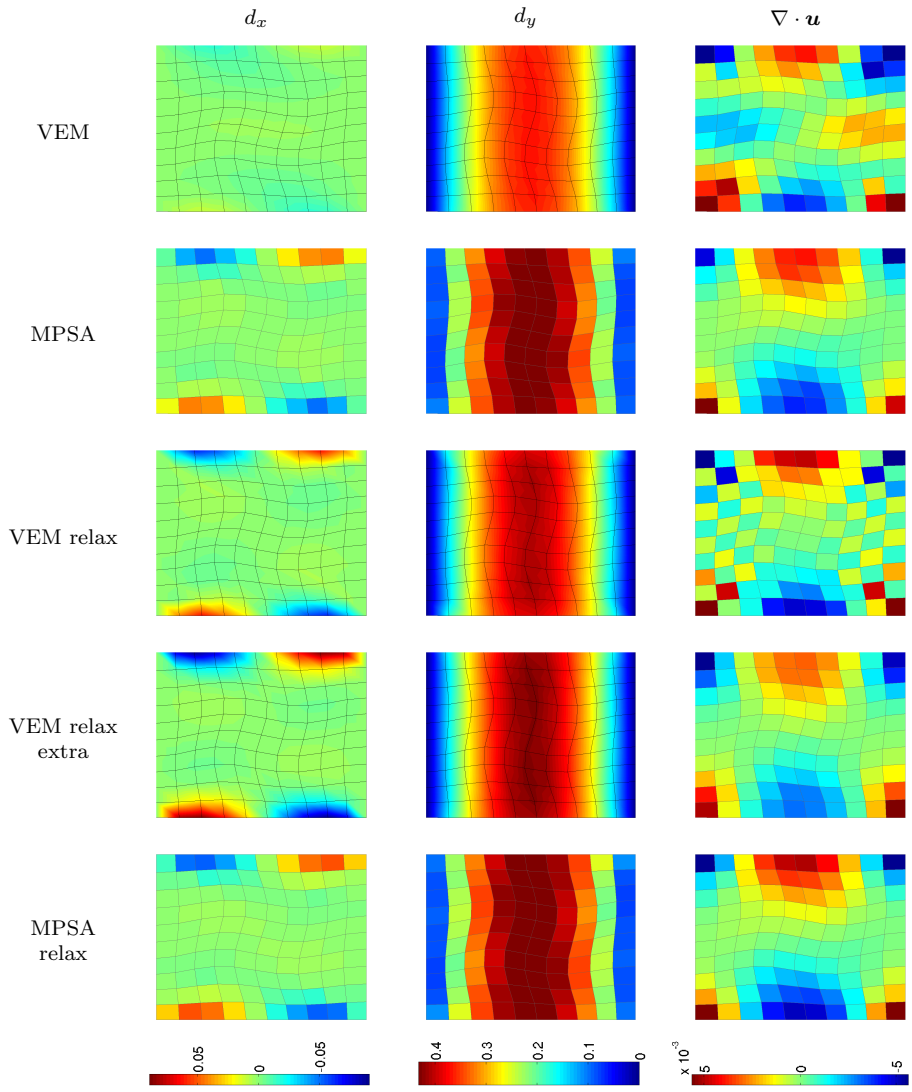

Fig. 27 Quadrilateral grid and $\nu = 0.495$ (Case 5c). VEM and VEM-relax suffer from numerical locking. MPSA does not present any sign of locking. VEM-relax-extra is free from locking, as predicted by the theory

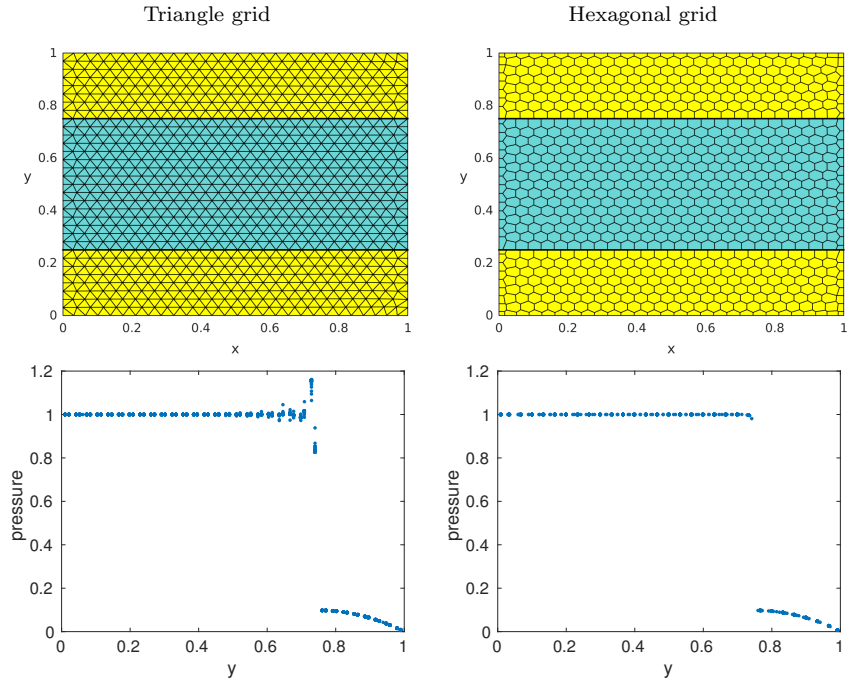

Fig. 28 This figure presents the result for the simulation of Biot's equation (case 6). We consider a triangle grid (left) and hexagonal grid (right), where the yellow region has high permeability (1) while the other color indicate low permeability (10^{-5}). In the lower row, we show the pressure as a function of the vertical position, after one time step simulation. We use VEM-relax. We can observe how the numerical locking, in the case of the triangle grid, introduces artificial pressure oscillations. In comparison, the hexagonal grid which prevents locking yields an oscillation free pressure field.

4 Conclusion

In this paper, we have tested the behaviors of the VE and MPSA methods for linear elasticity with respect to grid features and parameter values that are typical to subsurface models. We can conclude that both methods are capable to handle in a satisfactory manner the polyhedral grid structures that are standard in such models. A priori, both methods have relative advantages. The MPSA method is attractive from the physical point of view, due to the explicit treatment of the force continuity at the cell interfaces. The MPSA offers a natural stable coupling with poro-elasticity, see [23]. From the implementation point of view, the MPSA method is cell-centered and therefore shares the same grid structure as the MPFA method, which is also often the preferred convergent method for multi-phase flow. The VE method has the advantage of robustness. Obtained from a variational principle applied to an energy norm, it leads automatically to a symmetric positive definite system of equations which guarantees the robustness of the method. For simplexes, the method reduces to the finite element method so that the large collection of techniques developed for finite elements, such as preconditioning, super-convergence techniques or patch recovery can be relatively easily applied to VEM. When we use the approach presented in [10] as we do in this paper, the projection operators are given explicitly and do not require extra local computations as they usually do in a VE method, so that the local assembly has finally the same structure as in the traditional finite element method. If one is interested in generating the deformed grid obtained from a computed displacement field, another advantage of the VE method is that that the deformed grid can be readily constructed as the method yields nodal displacement. In comparison, the MPSA method requires an extra post-processing step and the task of generating a deformed grid from displacements at cell centers is not trivial. There is no explicit reconstruction of continuous displacement field from values given at cells.

In geological models, the convergence properties of a method are not as important as its performance on coarse and strongly irregular meshes. In a first series of test, we have checked the convergence of the method for randomly perturbed quadrilateral grids. Then, we studied the behavior of the method on strongly distorted grid and grids with high aspect ratio. At this stage, we reached the limit of both methods. For the MPSA, we exceeded the grid restriction of the method. The VE method is robust but convergence is guaranteed with a uniform bound on the aspect ratio. At high aspect ratio, it was therefore not surprising that we observe discrepancies of the solutions.

We have studied the behavior of both methods for grids containing two regions with different refinements (cases 3). The first conclusion is that both methods are robust with respect to the refinement ratio in averaged norms (L^2 norms). As the refinement ratio is increased, oscillations in the forces at the interaction region appear for the VE method and, in the case of isotropic refinement (case 3a), the local values for the stress even blow-up. We interpret this behavior by the highly non-linear nature of the virtual basis in this case.

The freedom we have in choosing the regularization term in VEM could be used to dampen these unwanted effects but we do not explore this possibility in this paper. The MPSA does not present the same level of oscillations in the force term and yields more reliable values for the forces, which is in accordance with the fact that the method is based on a force continuity principle. We have studied the behavior of the methods in the case of a thin layer (case 4). The conclusion is that both methods are robust with respect to the thickness of the layer. When the layer is refined, the VE method introduces, as previously, oscillation in the forces at the interface but also in the divergence term inside the layer. The error term in the divergence remained confined to the layer in VEM while it is spread for MPSA.

Even if the rocks considered in a subsurface model are far from being incompressible, the coupling with fluid flow requires that the methods used for elasticity are robust with respect to the incompressible limit and, in particular, not sensitive to numerical locking. We have conducted tests for both methods (Case 5). First, we confirm the intuition that the MSPA and VEM methods have opposite responses to numerical locking depending on the grid structure: In VEM, numerical locking will appear for grids with relatively more cells than nodes (such as triangular grids) and, in MPSA, it will appear for grids with relatively more nodes than cells (such as hexagonal grids). We can get rid of numerical locking for VEM using established theory, as presented in [5] for the Stokes problem, by relaxing the divergence term and adding extra degrees of freedom. For MPSA, by introducing an extra degree of freedom at cell center, which correspond to pressure, it is also possible to derive a method that is robust with respect to locking. All these methods have been tested and the regularized methods fulfill the expectation we have concerning locking. Moreover, we can conclude from our experiments that, using the standard versions, the MPSA method seems more robust than the VE method with respect to locking. For example, MPSA can handle quadrilateral grids where VEM fails.

Acknowledgements We thank Odd Anderson from SINTEF ICT in Oslo for his help to set up the numerical test case for the Biot model.

References

[1] I. Aavatsmark. “An introduction to multipoint flux approximations for quadrilateral grids”. In: *Comput. Geosci.* 6 (2002), pp. 405–432.

[2] L. Agélas, C. Guichard, and R. Masson. “Convergence of finite volume MPFA O type schemes for heterogeneous anisotropic diffusion problems on general meshes”. In: *International Journal on Finite Volumes* (2010), volume–7.

[3] D. N. Arnold, F. Brezzi, and J. Douglas. “PEERS: A new mixed finite element for plane elasticity”. In: *Japan Journal of Applied Mathematics* 1.2 (1984), pp. 347–367.

[4] L. Beirão da Veiga, F. Brezzi, and L. D. Marini. "Virtual elements for linear elasticity problems". In: *SIAM Journal on Numerical Analysis* 51.2 (2013), pp. 794–812.

[5] L. Beirão da Veiga, K. Lipnikov, and G. Manzini. *Mimetic Finite Difference Method for Elliptic Problems*. Vol. 11. Springer, 2014.

[6] L. Beirão da Veiga et al. "Basic principles of virtual element methods". In: *Mathematical Models and Methods in Applied Sciences* 23.01 (2013), pp. 199–214.

[7] M. A. Biot. "General theory of three-dimensional consolidation". In: *Journal of applied physics* 12.2 (1941), pp. 155–164.

[8] F. Brezzi, K. Lipnikov, and M. Shashkov. "Convergence of the mimetic finite difference method for diffusion problems on polyhedral meshes". In: *SIAM Journal on Numerical Analysis* 43.5 (2005), pp. 1872–1896.

[9] F. Brezzi, K. Lipnikov, and V. Simoncini. "A family of mimetic finite difference methods on polygonal and polyhedral meshes". In: *Mathematical Models and Methods in Applied Sciences* 15.10 (2005), pp. 1533–1551.

[10] A. L. Gain, C. Talischi, and G. H. Paulino. "On the Virtual Element Method for three-dimensional linear elasticity problems on arbitrary polyhedral meshes". In: *Computer Methods in Applied Mechanics and Engineering* 282 (2014), pp. 132–160.

[11] J. B. Haga, H. Osnes, and H. P. Langtangen. "On the causes of pressure oscillations in low-permeable and low-compressible porous media". In: *International Journal for Numerical and Analytical Methods in Geomechanics* 36.12 (2012), pp. 1507–1522.

[12] E. Keilegavlen and J. M. Nordbotten. "Finite volume methods for elasticity with weak symmetry". In: *International Journal for Numerical Methods in Engineering* (2017). NME-Jul-16-0496.R2, n/a–n/a. ISSN: 1097-0207. URL: http://dx.doi.org/10.1002/nme.5538.

[13] R. A. Klausen and R. Winther. "Convergence of multipoint flux approximations on quadrilateral grids". In: *Numerical methods for partial differential equations* 22.6 (2006), pp. 1438–1454.

[14] R. A. Klausen and R. Winther. "Robust convergence of multi point flux approximation on rough grids". In: *Numerische Mathematik* 104.3 (2006), pp. 317–337.

[15] K.-A. Lie et al. "Open source MATLAB implementation of consistent discretisations on complex grids". In: *Comput. Geosci.* 16 (2 2012), pp. 297–322. ISSN: 1420-0597.

[16] K. Lipnikov, G. Manzini, and M. Shashkov. "Mimetic finite difference method". In: *Journal of Computational Physics* 257 (2014), pp. 1163–1227.

[17] K. Lipnikov, M. Shashkov, and I. Yotov. "Local flux mimetic finite difference methods". In: *Numerische Mathematik* 112.1 (2009), pp. 115–152.

[18] *The MATLAB Reservoir Simulation Toolbox, Version 2016a*. July 2016. URL: http://www.sintef.no/MRST/.

[19] J. C. Nagtegaal, D. M. Parks, and J. Rice. "On numerically accurate finite element solutions in the fully plastic range". In: *Computer methods in applied mechanics and engineering* 4.2 (1974), pp. 153–177.

[20] H. M. Nilsen, K.-A. Lie, and J. R. Natvig. "Accurate modelling of faults by multipoint, mimetic, and mixed methods". In: *SPE J.* 17.2 (2012), pp. 568–579.

[21] J. M. Nordbotten. "Cell-centered finite volume discretizations for deformable porous media". In: *International Journal for Numerical Methods in Engineering* 100.6 (2014), pp. 399–418.

[22] J. M. Nordbotten. "Convergence of a Cell-Centered Finite Volume Discretization for Linear Elasticity". In: *SIAM Journal on Numerical Analysis* 53.6 (2015), pp. 2605–2625.

[23] J. M. Nordbotten. "Stable cell-centered finite volume discretization for Biot equations". In: *SIAM Journal on Numerical Analysis* 54.2 (2016), pp. 942–968.

[24] X. Raynaud, H. M. Nilsen, and O. Andersen. "Virtual element method for geomechanical simulations of reservoir models". In: *ECMOR XV–15th European Conference on the Mathematics of Oil Recovery, Amsterdam, Netherlands*. 2016.

[25] X. Raynaud, H. M. Nilsen, and O. Andersen. "Virtual Element Method for geomechanics on reservoir grids". In: *ArXiv e-prints* (Feb. 2017). arXiv: 1606.09508v2 [math.NA].

[26] O. C. Zienkiewicz and J. Z. Zhu. "The superconvergent patch recovery and a posteriori error estimates. Part 1: The recovery technique". In: *International Journal for Numerical Methods in Engineering* 33.7 (1992), pp. 1331–1364. ISSN: 1097-0207.